

See discussions, stats, and author profiles for this publication at: <https://www.researchgate.net/publication/245426337>

Noise Generation in the Near-Nozzle Region of a Chevron Nozzle Jet Flow

Article in *AIAA Journal* · August 2009

DOI: 10.2514/1.36659

CITATIONS

115

READS

458

2 authors, including:

[Mohammed Yousuff Hussaini](#)

Florida State University

459 PUBLICATIONS 23,288 CITATIONS

[SEE PROFILE](#)

Some of the authors of this publication are also working on these related projects:



HIV Optimal Control [View project](#)



Wall-Resolved Large-Eddy Simulations of High-Reynolds Number Separated Flows [View project](#)

Simulation of Noise Generation in Near-Nozzle Region of a Chevron Nozzle Jet

Ali Uzun* and M. Yousuff Hussaini†

Florida State University, Tallahassee, Florida 32306-4510

DOI: 10.2514/1.36659

This paper reports on the simulation of the near-nozzle region of a moderate Reynolds number cold jet flow exhausting from a chevron nozzle. The chevron nozzle considered in this study is the SMC001 nozzle experimentally studied by researchers at the NASA John H. Glenn Research Center. This nozzle design contains six symmetric chevrons that have a 5-deg penetration angle. The flow inside the chevron nozzle and the free jet flow outside are computed simultaneously by a high-order accurate, multiblock, large-eddy simulation code with overset grid capability. The resolution of the simulation is about 100 million grid points. The main emphasis of the simulation is to capture the enhanced shear-layer mixing due to the chevrons and the consequent noise generation that occurs in the mixing layers of the jet within the first few diameters downstream of the nozzle exit. Details of the computational methodology are presented together with an analysis of the simulation results. The simulation data are compared with available experimental measurements of the flowfield and the noise spectrum in the sideline direction. Overall, the simulation results are very encouraging and demonstrate the feasibility of chevron nozzle jet computations using our simulation methodology.

Nomenclature

c	= sound speed
D	= spatial derivative
D_j	= jet nozzle diameter
e_t	= total energy, $\rho(u^2 + v^2 + w^2)/2 + p/(\gamma - 1)$
$\mathbf{F}, \mathbf{G}, \mathbf{H}$	= inviscid flux vectors in Navier–Stokes equations
$\mathbf{F}_v, \mathbf{G}_v, \mathbf{H}_v$	= viscous flux vectors in Navier–Stokes equations
f	= arbitrary variable; frequency
i, j, k	= grid point indices
J	= metric Jacobian
L	= 50% correlation length scale
N	= number of grid points along given spatial direction
p	= static pressure
Q	= vector of conservative flow variables
Q	= Q/J
Re_D	= jet nozzle Reynolds number, $\rho_j U_j D_j / \mu_j$
Re_θ	= momentum thickness Reynolds number, $\rho_j U_j \delta_\theta / \mu_j$
\mathcal{R}_{rr}	= two-point velocity correlation in radial direction
$\mathcal{R}_{\lambda\lambda}$	= two-point velocity correlation in λ direction
Sr_D	= Strouhal number, $f D_j / U_j$
t	= time
U	= mean axial or streamwise velocity
u_τ	= friction velocity, $\sqrt{\tau_{\text{wall}} / \rho_{\text{wall}}}$
u, v, w	= Cartesian velocity components in x, y , and z directions
v_λ	= velocity component in λ direction
v_r	= velocity component in radial direction
x, y, z	= Cartesian coordinates

α_f	= filtering parameter
γ	= ratio of specific heats of air, 1.4
Δ_r	= wall-normal or radial grid spacing
Δ_θ	= azimuthal grid spacing
Δ_x	= axial or streamwise grid spacing
Δt	= time increment
$\Delta \xi$	= uniform grid spacing along ξ direction in the computational domain
δ	= boundary-layer or shear-layer thickness
δ_{exit}	= boundary-layer thickness at cylindrical pipe exit
δ_{inlet}	= boundary-layer thickness at cylindrical pipe inlet
δ_θ	= momentum thickness of boundary layer
ϵ_f	= artificial dissipation parameter in implicit time stepping
μ	= molecular viscosity
ν	= kinematic viscosity, μ / ρ
ξ, η, ζ	= generalized curvilinear coordinates
ρ	= fluid density
σ_{ijk}	= spectral radius of inviscid flux Jacobian at grid point (i, j, k)
τ	= wall shear stress; time scale
$\langle \rangle$	= time averaging operator

Subscripts

i	= value at grid point i
j	= value at nozzle exit centerline
r	= radial direction
wall	= value on wall
x	= axial or streamwise direction
θ	= azimuthal direction; value based on momentum thickness
λ	= periodic direction along which mean axial velocity is constant
∞	= ambient value

Superscripts

B	= backward operator in prefactored optimized compact scheme
F	= forward operator in prefactored optimized compact scheme
n	= time level
p	= subiteration level

Presented as Paper 3596 at the 13th AIAA/CEAS Aeroacoustics Conference, Rome, Italy, 21–23 May 2007; received 14 January 2008; revision received 5 August 2008; accepted for publication 12 August 2008. Copyright © 2008 by the authors. Published by the American Institute of Aeronautics and Astronautics, Inc., with permission. Copies of this paper may be made for personal or internal use, on condition that the copier pay the \$10.00 per-copy fee to the Copyright Clearance Center, Inc., 222 Rosewood Drive, Danvers, MA 01923; include the code 0001-1452/09 \$10.00 in correspondence with the CCC.

*Research Associate, Program in Computational Science and Engineering. Senior Member AIAA.

†Sir James Lighthill Professor, Program in Computational Science and Engineering. Fellow AIAA.

- = spatially filtered quantity
- + = value given in wall units
- / = perturbation from mean value
- ~ = Favre-filtered quantity

I. Introduction

JET noise reduction is one of the major issues concerning jet engine manufacturers. Environmental concerns and strict noise regulations around major airports have made jet noise a crucial problem in present day aeroacoustics research, as it is the jet engine exhaust that is responsible for most of the noise generation during aircraft takeoff. The importance of the problem has motivated numerous experimental and computational studies to date. Current jet noise research is directed toward three main areas: improvement in noise prediction tools, better understanding of the underlying noise generation mechanisms, and investigation of various noise reduction devices such as tabs, chevrons, microjet injection, and lobed mixers.

Chevron nozzles have drawn a lot of attention recently due to their noise reduction benefits and are currently one of the most popular jet noise reduction devices. Chevrons typically reduce the low-frequency noise at aft angles, whereas they increase the high-frequency noise at broadside angles relative to the jet [1]. The streamwise vorticity generated by the chevrons enhances mixing in the shear layers of the jet, which leads to a decrease or increase in noise over certain frequency ranges. The ultimate goal in chevron design is to decrease the low-frequency noise as much as possible while preventing a significant increase in high-frequency noise. Some of the parameters that can be varied for this problem are the chevron count, chevron penetration, and chevron length. Chevron count controls the spacing between the axial vortices generated by the chevrons, whereas chevron penetration controls the strength of the axial vorticity and chevron length controls the distribution of vorticity within the axial vortices [1]. Thus, an optimization study of several parameters is necessary to get the maximum amount of noise reduction with chevron nozzles.

It appears that experimental studies of chevron nozzles still use, more or less, a trial-and-error approach, because the effects of chevrons on the flow modification in the near-nozzle region are still not clearly understood. Moreover, the absence of a large experimental database for chevron nozzles makes it difficult to extrapolate the noise from existing experimental measurements to new chevron nozzle designs. Although experiments are necessary and provide useful data for validating the computations, they are expensive and can supply a relatively limited amount of information. Thus, computational methods are attractive for studying various chevron nozzle designs in a more cost-effective manner.

Several Reynolds-averaged Navier–Stokes (RANS) type computational studies (for example, see the works of Engblom et al. [2], Birch et al. [3], and Massey et al. [4]) have been conducted for chevron nozzles. The work of Engblom et al. [2] showed the deficiencies of the popular Mani–Gliebe–Balsa–Khavaran (MGBK) method [5,6] when applied to chevron nozzle noise prediction. It was also demonstrated by Birch et al. [3] that the RANS-based jet noise prediction procedure they employed could not fully account for the effect of chevrons on a jet, and thus a new noise source term, for which the underlying physical mechanism is still unclear, had to be added for the accurate prediction of the high-frequency part of the noise spectra. On the other hand, large-eddy simulation (LES) has the capability to provide much more detailed information about the nature of the flow alteration caused by the chevrons in the near-nozzle region. The first LES-type computations for chevron nozzle jets seems to be have been performed by Shur et al. [7,8] with good success. It is worth mentioning here that the chevron nozzle geometry was not explicitly included in their simulations. Instead, a chevron emulation procedure, for which the details can be found in their papers, was used to represent the shape of the initial mixing layer on the inflow boundary of the free jet flow. Although they demonstrated that LES is quite promising in the successful prediction of the relatively low-frequency part of the noise spectra (up to a

Strouhal frequency of 4), the prediction of higher frequencies via LES still remains a challenge.

In the present study, we perform reasonably well-resolved numerical computations of both chevron nozzle and free jet flows in the near-nozzle region and explore how well the near-nozzle high-frequency noise generation due to enhanced shear-layer mixing induced by the chevrons is captured. It has been previously shown that the multiblock and overset capabilities of the present LES code provide flexibility in meshing complex computational domains while allowing grid density control in various regions [9,10]. High-order accurate schemes ensure a high-quality numerical solution whereas implicit time stepping brings great savings in computing cost. Unlike the emulation approach of Shur et al. [7,8], the chevron nozzle geometry to be considered in this study is explicitly included in the computational grid. The multiblock and overset grid capabilities of the flow solver provide the flexibility of including any type of chevron nozzle geometry within the computational grid system. An inflow generation technique similar to that of Lund et al. [11] is applied to generate realistic inflow conditions at the nozzle inlet. The details of our simulation methodology are presented in the next section.

II. Computational Methodology

In this study, the Favre-filtered, unsteady, compressible, nondimensional Navier–Stokes equations formulated in curvilinear coordinates, which are expressed in the following conservative form, are solved:

$$\frac{\partial \mathbf{Q}}{\partial t} = - \left[\frac{\partial}{\partial \xi} \left(\frac{\mathbf{F} - \mathbf{F}_v}{J} \right) + \frac{\partial}{\partial \eta} \left(\frac{\mathbf{G} - \mathbf{G}_v}{J} \right) + \frac{\partial}{\partial \zeta} \left(\frac{\mathbf{H} - \mathbf{H}_v}{J} \right) \right] \quad (1)$$

Here, t is the time, ξ , η , and ζ are the generalized curvilinear coordinates of the computational space, and J is the Jacobian of the coordinate transformation from the physical domain to the computational domain. $\mathbf{Q} = \mathbf{Q}/J$ where $\mathbf{Q} = [\bar{\rho}, \bar{\rho} \tilde{u}, \bar{\rho} \tilde{v}, \bar{\rho} \tilde{w}, \bar{\rho} \tilde{e}]^T$ is the vector of conservative flow variables; \mathbf{F} , \mathbf{G} , and \mathbf{H} are the inviscid flux vectors; and \mathbf{F}_v , \mathbf{G}_v , and \mathbf{H}_v are the viscous flux vectors. The details of the governing equations can be found in Rizzetta et al. [12] or in Uzun [13].

A single-block LES code that was previously developed by Uzun et al. [13–15] has been extended to a multiblock version. Gaitonde and Visbal [16,17] have investigated multiblock implementation strategies in which high-order compact schemes are simultaneously employed in every subdomain, and grid point overlaps are used to exchange data between adjacent subdomains during the course of the computations. The attractiveness of this technique is that it allows high-order accurate simulations to be performed in complex domains using multiblock structured grids. A multiblock implementation strategy similar to that of Gaitonde and Visbal [16] is incorporated in the multiblock version of the LES code with a seven-point grid overlap between neighboring blocks. The standard Message Passing Interface library routines have been used in the code parallelization.

We now consider an individual block of the multiblock grid. The nonuniformly spaced curvilinear grid in physical space is transformed to a uniform grid in computational space, and the discretized governing equations are solved on the uniform grid. High-order compact finite difference schemes are used to compute the spatial derivatives in the governing equations. The fourth-order optimized prefactored compact schemes developed by Ashcroft and Zhang [18] offer improved dispersion characteristics compared to the standard sixth- and eighth-order compact schemes [19]. The prefactorization strategy splits the central implicit schemes into forward and backward biased operators.

The prefactored optimized schemes require the solution of two independent bidiagonal matrices. The spatial derivative at a given grid point i is given by

$$D_i = \frac{1}{2}(D_i^F + D_i^B) \quad (2)$$

where D_i^F and D_i^B represent the forward and backward operators, respectively. The prefactored compact scheme we use is a fourth-

order scheme with a five-point stencil. Hence, the forward and backward operators are given as follows:

$$\frac{1}{2}D_i^F = \frac{1}{2\beta\Delta\xi}[b(f_{i+1} - f_i) + d(f_{i-1} - f_i) + e(f_{i-2} - f_i)] - \frac{\alpha}{2\beta}D_{i+1}^F \quad (3)$$

$$\frac{1}{2}D_i^B = \frac{1}{2\beta\Delta\xi}[b(f_i - f_{i-1}) + d(f_i - f_{i+1}) + e(f_i - f_{i+2})] - \frac{\alpha}{2\beta}D_{i-1}^B \quad (4)$$

where the coefficients α , β , b , d , and e are given by Ashcroft and Zhang [18], f_i denotes the value of f (the quantity for which the spatial derivative is being computed) at grid point i , and $\Delta\xi$ is the uniform grid spacing along a given spatial direction in the computational space.

The preceding scheme is applicable to grid points $i = 3$ through $i = N - 2$, where N is the number of grid points along the spatial direction. Additional boundary stencils are required at grid points $i = 1, 2$, and $i = N - 1, N$. The third-order boundary stencils we use are given by Ashcroft and Zhang [18]. At grid points $i = 2$ and $i = N - 1$, the following explicit backward and forward stencils are used:

$$D_2^B = \frac{1}{\Delta\xi} \sum_{i=1}^4 s_i f_i, \quad D_{N-1}^B = \frac{1}{\Delta\xi} \sum_{i=N-3}^N e_i f_i \quad (5)$$

$$D_2^F = \frac{1}{\Delta\xi} \sum_{i=1}^4 -e_{N+1-i} f_i, \quad D_{N-1}^F = \frac{1}{\Delta\xi} \sum_{i=N-3}^N -s_{N+1-i} f_i \quad (6)$$

The coefficients $s_i (i = 1, \dots, 4)$ and $e_i (i = N - 3, \dots, N)$ are given by Ashcroft and Zhang [18]. At grid points $i = 1$ and $i = N$, the following one-sided explicit schemes are employed to compute the spatial derivative:

$$D_1 = \frac{1}{\Delta\xi} \sum_{i=1}^4 c_i f_i, \quad D_N = \frac{1}{\Delta\xi} \sum_{i=N-3}^N -c_{N+1-i} f_i \quad (7)$$

where $c_1 = -\frac{33}{18}$, $c_2 = 3$, $c_3 = -\frac{3}{2}$, and $c_4 = \frac{1}{3}$.

The viscous stress terms appearing in the governing equations are obtained using the first-derivatives of the velocity components. The spatial derivatives of the inviscid and viscous flux vectors are computed using the prefactored optimized compact scheme. As a consequence of such an implementation, the second derivatives in the viscous fluxes are essentially evaluated by the application of the first-derivative operator twice. Although this approach is not as accurate as when a compact scheme is used to directly compute the second derivatives in the viscous terms, it is much cheaper to implement in curvilinear coordinates. We should also note here that, for computational efficiency, the terms in the inviscid and viscous fluxes can be added together and then the total flux can be differentiated. However, the characteristic-type boundary conditions implemented on solid walls (to be discussed shortly) require the separation of inviscid and viscous fluxes, hence we compute the inviscid and viscous flux derivatives separately.

The LES code also employs the following sixth-order tridiagonal spatial filter used by Visbal and Gaitonde [17]:

$$\alpha_f \bar{f}_{i-1} + \bar{f}_i + \alpha_f \bar{f}_{i+1} = \sum_{n=0}^3 \frac{a_n}{2} (f_{i+n} + f_{i-n}) \quad (8)$$

where \bar{f}_i denotes the filtered value of quantity f at grid point i , and

$$\begin{aligned} a_0 &= \frac{11}{16} + \frac{5\alpha_f}{8}, & a_1 &= \frac{15}{32} + \frac{17\alpha_f}{16} \\ a_2 &= \frac{-3}{16} + \frac{3\alpha_f}{8}, & a_3 &= \frac{1}{32} - \frac{\alpha_f}{16} \end{aligned} \quad (9)$$

The parameter α_f must satisfy the inequality $-0.5 < \alpha_f < 0.5$. A less dissipative filter is obtained with higher values of α_f within the given range. With $\alpha_f = 0.5$, there is no filtering effect, because Eq. (8) reduces to an identity.

Because this filter has a seven-point right-hand side stencil, it obviously cannot be used at near-boundary points. Instead, the following sixth-order equation with a one-sided right-hand side stencil is used at grid points near the left boundary point $i = 1$:

$$\alpha_f \bar{f}_{i-1} + \bar{f}_i + \alpha_f \bar{f}_{i+1} = \sum_{n=1}^7 a_{n,i} f_n \quad (i = 2, 3) \quad (10)$$

where the coefficients $a_{n,i}$ are given by Visbal and Gaitonde [17]. For the points near the right boundary point $i = N$, we apply a similar formulation [17]. The boundary points $i = 1$ and $i = N$ are left unfiltered.

The filtering process eliminates spurious high-frequency numerical oscillations and ensures numerical stability. Numerical tests show that values of the filtering parameter α_f between 0.45 and 0.49 effectively eliminate spurious oscillations while providing very little dissipation and, hence, leave the well-resolved scales mostly unaffected. A value of $\alpha_f = 0.47$, which is in the middle of this range, has been used in the present simulation. The value of α_f is rather insensitive to flow parameters such as Reynolds number and Mach number, or other parameters like the domain size and number of grid points. We have used the value of $\alpha_f = 0.47$ for a variety of problems and this value has provided sufficient numerical stability with little dissipation for all the different problems we have studied.

Time advancement can be performed by means of either the standard fourth-order, four-stage explicit Runge–Kutta scheme or a second-order Beam–Warming-type implicit time integration scheme [20,21]. The iterative form of the approximately factored finite difference algorithm of Beam and Warming [20] that is second-order accurate in time can be represented as

$$\begin{aligned} & \left[\mathbf{I} + \frac{2\Delta t}{3} \frac{\partial}{\partial \xi} \left(\frac{\partial \mathbf{F}}{\partial \mathbf{Q}} - \frac{\partial \mathbf{F}_v}{\partial \mathbf{Q}} \right) \right]^p \times \left[\mathbf{I} + \frac{2\Delta t}{3} \frac{\partial}{\partial \eta} \left(\frac{\partial \mathbf{G}}{\partial \mathbf{Q}} - \frac{\partial \mathbf{G}_v}{\partial \mathbf{Q}} \right) \right]^p \\ & \times \left[\mathbf{I} + \frac{2\Delta t}{3} \frac{\partial}{\partial \zeta} \left(\frac{\partial \mathbf{H}}{\partial \mathbf{Q}} - \frac{\partial \mathbf{H}_v}{\partial \mathbf{Q}} \right) \right]^p \Delta \mathbf{Q}^p \\ & = - \left[\mathbf{Q}^p - \frac{4}{3} \mathbf{Q}^n + \frac{1}{3} \mathbf{Q}^{n-1} \right] - \frac{2\Delta t}{3} \left[\frac{\partial}{\partial \xi} (\mathbf{F} - \mathbf{F}_v) \right. \\ & \left. + \frac{\partial}{\partial \eta} (\mathbf{G} - \mathbf{G}_v) + \frac{\partial}{\partial \zeta} (\mathbf{H} - \mathbf{H}_v) \right]^p \end{aligned} \quad (11)$$

The superscript p denotes the subiteration level, \mathbf{I} represents the identity matrix, Δt is the time step, and $\Delta \mathbf{Q}^p = \mathbf{Q}^{p+1} - \mathbf{Q}^p$. For $p = 1$, $\mathbf{Q}^p = \mathbf{Q}^n$, where n represents the current time level, and $n - 1$ represents the previous time level. \mathbf{Q}^{p+1} is the $p + 1$ approximation to the solution at the $n + 1$ time level, \mathbf{Q}^{n+1} .

After several subiterations at each time step, $\Delta \mathbf{Q}^p$ converges toward a very small value. A second-order accurate, three-point scheme is used to calculate the time derivative on the right-hand side of Eq. (11). It is well known that, although the Beam–Warming scheme [20] is unconditionally stable in two dimensions, it becomes unstable in three dimensions. To conditionally stabilize the scheme for the 3-D computations, we make use of artificial dissipation [22] in the implicit side of Eq. (11). For example, while applying the equation along the ξ direction, the artificial dissipation operator is appended to the implicit operator as follows:

$$\begin{aligned} & \left[\mathbf{I} + \frac{2\Delta t}{3} \frac{\partial}{\partial \xi} \left(\frac{\partial \mathbf{F}}{\partial \mathbf{Q}} - \frac{\partial \mathbf{F}_v}{\partial \mathbf{Q}} \right) - \epsilon_I \nabla_\xi (\sigma_{i+1,j,k} J_{i+1,j,k}^{-1} \right. \\ & \left. + \sigma_{i,j,k} J_{i,j,k}^{-1}) \Delta_\xi J \right]^p \end{aligned} \quad (12)$$

where $\nabla_\xi f_{i,j,k} = f_{i,j,k} - f_{i-1,j,k}$, $\Delta_\xi f_{i,j,k} = f_{i+1,j,k} - f_{i,j,k}$, $\sigma_{i,j,k}$ is the spectral radius of the inviscid flux Jacobian $(\partial \mathbf{F} / \partial \mathbf{Q})$ at grid point (i, j, k) , and ϵ_I controls the strength of the artificial dissipation. It was

found that $\epsilon_f = 0.5\Delta t$ provides adequate artificial dissipation to maintain stability.

We should also note here that the somewhat cumbersome evaluation of the viscous flux Jacobians in generalized curvilinear coordinates is skipped in this work. Our experience shows that, as several subiterations are applied per time step, neglecting the viscous flux Jacobians does not negatively impact the convergence of the scheme. The spatial derivatives operating on the fluxes on the right-hand side are computed using the prefactored optimized compact scheme described previously. On the other hand, the spatial derivatives operating on the flux Jacobians on the left-hand side are computed using the fourth-order compact scheme from Lele [19]. Use of compact schemes to attain high-order spatial accuracy for the implicit operators was originally proposed by Ekaterinaris [21]. The implicit time stepping algorithm we have implemented then becomes truly second-order accurate in time and fourth-order accurate in space.

Application of compact schemes for the implicit operators results in a block tridiagonal matrix system along each of the three computational directions, which are solved sequentially as described by Ekaterinaris [21]. This procedure basically replaces the three-dimensional problem by three one-dimensional problems at a given time level. Numerical experiments have shown that, typically, two or three subiterations per time step are sufficient to reduce the errors due to approximate factorization, linearization, and artificial dissipation, and consequently drive ΔQ^p toward small values at each time step. The solution is filtered after every subiteration to ensure numerical stability. Because of the repeated application of filtering to maintain stability, ΔQ^p does not become exactly zero. However, numerical tests show that, after few subiterations, ΔQ^p attains a value that is at least several orders of magnitude smaller relative to its initial value which is obtained at the first subiteration.

In the present study, we attach a cylindrical pipe upstream of the conical chevron nozzle and employ a procedure similar to that of Lund et al. [11] in an attempt to generate fully turbulent boundary layers at the cylindrical pipe inlet. The method of Lund et al. [11] was originally developed for generating three-dimensional, time-dependent turbulent inflow data for spatially developing zero-pressure-gradient incompressible boundary layers. In this approach, instantaneous planes of velocity data are extracted at a specified location downstream of the inlet boundary. The velocity field is then rescaled according to boundary-layer similarity laws and reintroduced at the inlet. The streamwise pressure gradient in a cylindrical pipe flow, although not strictly equal to zero, is only weakly favorable. Hence, we expect the method of Lund et al. [11] to work reasonably well for the turbulent inflow boundary-layer generation in a cylindrical pipe flow as well.

Because implicit time stepping is used in the present simulation, the inflow conditions at the nozzle inlet are specified in terms of time derivatives. The rescaling-recycling procedure determines the solution to be imposed on the inlet boundary at the future time step $n + 1$. The solution at the current time step n and the previous time step $n - 1$ is already known. Using the flow solution at three time levels, we can use the following approximation to specify the time derivative of the solution at the inlet boundary:

$$\left(\frac{\partial Q}{\partial t}\right)_{\text{inlet}} = \frac{3Q^{n+1} - 4Q^n + Q^{n-1}}{2\Delta t} \quad (13)$$

Now, looking at Eqs. (1) and (11), it is easy to see that the time derivative computed using this equation for the inlet boundary grid points can be used to overwrite the sum of the flux derivatives which appears in the right-hand side of Eq. (11). This is the way the cylindrical pipe inflow conditions are handled in the implicit time marching scheme.

It should also be reiterated that the method of Lund et al. [11] was originally developed for incompressible flows. However, the same method has been commonly used for recycling the velocity field in compressible flows as well (see, for example, the work of Sagaut et al. [23] for a review of the methods used in compressible flow). In this work, the mean velocity profile at the inlet is kept fixed and set to the

Spalding mean velocity profile [24]. Only the velocity fluctuations are recycled and reintroduced at the inlet. Additionally, for compressible flows, a rescaling law for two thermodynamic variables is needed. See the work of Sagaut et al. [23] for the various rescaling methods of thermodynamic variables used in compressible flow applications. In the present study, we keep pressure constant on the entire inflow boundary, and we recycle temperature using the same recycling method which Sagaut et al. [23] used. We do the temperature recycling only inside the boundary layer. Outside the boundary layer, temperature is set to a constant value. The two regions are then smoothly blended.

Admittedly, specification of pressure and temperature in this manner makes the cylindrical pipe inflow boundary a reflecting type of boundary. In acoustics applications, one would ideally like to impose only the velocity fluctuations on the inflow boundary and compute pressure and density (or temperature) using some kind of nonreflecting boundary condition. Our experience shows that this is extremely difficult, if not impossible, to achieve in practice. We experimented with several nonreflecting-type boundary conditions on the entire inflow boundary, while imposing only the velocity fluctuations computed using the rescaling-recycling procedure. However, numerical instability was observed in all of the cases we tried. We believe the problem is due to the interaction of strong velocity fluctuations in the boundary layer with the existing nonreflecting boundary-condition formulations. We also tried another approach in which the nonreflecting boundary condition was applied only outside the boundary layer, while the pressure and temperature inside the boundary layer were obtained from the rescaling-recycling procedure. However, trying to blend the nonreflecting part of the inflow boundary with the boundary-layer region was found to result in numerical instabilities as well.

Given these difficulties, our only choice was to adopt the aforementioned procedure. Nevertheless, in the present application, noise is generated exterior to the nozzle and propagates mostly in the lateral and downstream directions. Thus, we do not believe that there is significant acoustic wave reflection from the cylindrical pipe inflow boundary to have a strong impact on the results. A stable formulation of nonreflecting boundary conditions in combination with velocity perturbations computed using the inflow generation technique is highly desirable and can be an interesting topic for future research. Although we have attempted to generate fully turbulent boundary layers inside the cylindrical pipe, an analysis of the results later in this paper will provide evidence supporting the fact that the boundary layer entering the conical chevron nozzle is in a transitional rather than fully turbulent state. The fact that the boundary layer is not fully turbulent indicates problems with either the inflow generation method or the implicit LES (ILES) approach we are using (to be discussed shortly). However, as will be discussed soon, the ILES approach has been used successfully in wall-bounded problems by other researchers using numerical methods similar to the present one. Thus, we believe the inflow generation method is the primary suspect that is responsible for the lack of a fully turbulent boundary-layer development within the cylindrical pipe.

Tam and Dong radiation boundary conditions modified by Dong [25] are applied on the boundaries to which only acoustic disturbances are reaching. In contrast to the original Tam and Dong radiation boundary conditions [26], the Dong-modified radiation boundary conditions do not require any knowledge of the local mean flow on the radiation boundaries. Outflow boundaries are handled by characteristic-type outflow boundary conditions [27]. We additionally attach a sponge zone downstream of the physical domain and apply grid stretching in combination with artificial damping in this region to dissipate the turbulence in the flowfield before it reaches the outflow boundary. This way, unwanted numerical reflections from the outflow boundary are suppressed. On solid walls, a generalized characteristic-type solid wall boundary condition [28] is applied. The wall temperature is computed using either isothermal or adiabatic boundary conditions. Application of the boundary conditions when explicit time stepping is used is straightforward. In this case, on the boundary points, the residual on the right-hand side of Eq. (1) is simply overwritten by the boundary conditions. In the case of

implicit time stepping on the boundary points, the sum of the flux derivatives appearing on the right-hand side of Eq. (11) is replaced by the boundary conditions. Moreover, when solid wall boundaries are present, the block tridiagonal system of equations, which is solved during implicit time stepping, must be modified such that all velocity components on viscous walls are enforced to be zero.

At every time step, the solution is advanced independently in each block. Information is exchanged among the blocks at the end of each stage of the Runge–Kutta time integration scheme or after every directional sweep in each subiteration of the implicit time integration scheme, as well as after each application of the filter.

No explicit subgrid-scale (SGS) model is used in the present LES calculations. Instead, the spatial filter implemented in the LES is treated as an implicit SGS model. Thus, the approach we use here belongs to the implicit LES class of methods. It is well understood in turbulent flows that the energy cascade is associated with a mean flux of energy that is directed from large scales toward small scales. The large scales contain the major part of the turbulent kinetic energy and they continuously feed the turbulent kinetic energy via the cascade to the smallest eddies, where it is dissipated. Because the grid resolution in an LES is too coarse to resolve all of the relevant length scales, the accumulation of energy at the high wave numbers can be eliminated through the use of a spatial filter. Hence, the spatial filter can be thought of as an effective SGS model in an LES. In support of this observation, Visbal et al. [29,30] have performed LES of turbulent channel flow and compressible isotropic turbulence decay without using any explicit SGS model. In those simulations, they used high-order compact finite difference schemes and spatial filters similar to what we are using. Spatial filtering was treated as an implicit SGS model in their calculations. The ILES approach was found to produce acceptable results in the problems they studied. They also showed that the use of an SGS model in those simulations did not produce results superior to those obtained without employing an SGS model. The ILES approach has been successfully used by Sherer and Visbal [31] in turbulent channel flow computations as well.

We have also implemented overset grid capability into our multiblock LES code. The overset grid approach provides added flexibility in meshing domains around complex geometries and is useful for avoiding grid point singularities. In our past work, we have successfully used overset grids to avoid grid point singularities in the simulation of a round jet [9] and a wing tip vortex [10]. The reader is referred to these publications for the details of the overset grid systems used in these simulations.

It was previously shown by Sherer and Scott [32] that the use of second-order interpolation at overset grid boundaries results in a globally second-order accurate solution even when high-order compact differencing and filtering are used. Hence, we employ sixth-order accurate explicit Lagrangian interpolation in this work in conjunction with the high-order compact differencing and filtering schemes implemented in our code to ensure that a high-order accurate numerical solution is maintained throughout the entire computational domain. The sixth-order interpolation stencils are pre-computed by the Overset Grid Generator (OGEN) program (<http://www.llnl.gov/casc/Overture>) which was developed at the Lawrence Livermore National Laboratory. An intermediate program reads in the output of OGEN and reorganizes the data for use with our LES code. The 3-D interpolation stencil consists of seven points along each of the three computational coordinate directions. The interpolation process takes place in the computational space. We should also mention here that OGEN computes the location of the interpolation points within the computational space of a donor grid with only second-order accuracy. If sixth-order accuracy is desired in the interpolation process, then the location of the interpolation points within the computational space must be determined with sixth-order accuracy as well. For this purpose, a preprocessing program makes use of the interpolation stencils given by OGEN and computes the location of the interpolation points with sixth-order accuracy using a procedure described by Sherer and Scott [32].

Far-field noise computations are performed by coupling the time-accurate, unsteady near-field data provided by the LES with the

Ffowcs Williams–Hawkins (FWH) method [15,33]. In our implementation, we apply the FWH method on the fly, that is, while the LES is running and computing unsteady data on the FWH control surface. The additional subroutine included in the LES code for the application the FWH method on the fly requires negligible computing cost as compared with the main LES.

III. Test Case: Simulation of the Near-Nozzle Region of SMC001 Cold Jet

A. Simulation Details

We present results from the simulation of a cold jet exhausting from the SMC001 chevron nozzle configuration which is shown in Fig. 1. This chevron nozzle is one of the designs that was experimentally studied by researchers at the NASA John H. Glenn Research Center [1]. This design has six chevrons which penetrate the jet core flow by 5 deg. The acoustic Mach number of the jet centerline exit velocity is 0.9. This is the Mach number that is obtained using the ambient sound speed rather than the sound speed at the nozzle exit. The Reynolds number based on the jet nozzle exit centerline velocity and nozzle exit diameter is set to 100,000 in the simulation. The estimated Reynolds number of the experimental jet is around 1.4 million.

The Reynolds number of the LES is significantly lower than that of the experiment due to computational limitations. The Reynolds number difference between the computation and the experiment is expected to cause a mismatch of the initial shear-layer momentum thickness. Moreover, the initial turbulence intensity levels in the shear layer may also depend upon the Reynolds number. Such differences in the initial conditions may have important consequences on the development of the chevron jet mixing layer in the near-nozzle region. These issues will be discussed later when the computational results are compared with the experiment.

The main focus of the simulation is to compute the high-frequency noise generation in the near-nozzle region, thus the computational domain extends about 3.75 nozzle diameters downstream of the nozzle exit. The computational domain is discretized using multiblock and overset grids. A preliminary computation was performed using about 50 million grid points. However, an analysis of the acoustics results obtained on this grid revealed that more grid points are needed to properly resolve the high acoustic frequencies of interest. Thus, the grid was significantly refined in the radial direction, resulting in a new grid that contained about 100 million points total. The streamwise and azimuthal grid spacings in the new grid were kept the same as before.

The overset grid system used in the present simulation is topologically very similar to the overset grid system used in our previous



Fig. 1 Picture of the SMC001 chevron nozzle. (Taken from Engblom et al. [2].)

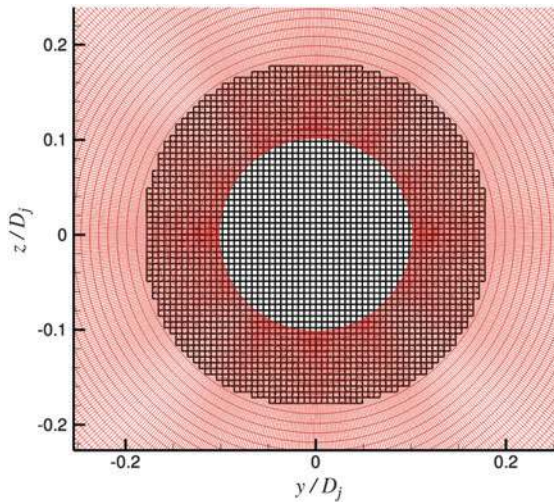


Fig. 2 Overset grid topology for the jet centerline region.

simulation of a jet exhausting from a round nozzle geometry [9]. To avoid the centerline singularity problem, we discretize the small region around the centerline of the jet using a relatively coarse rectangular grid, as can be seen in Fig. 2. Because the primary region of interest in this study does not contain the region near and downstream of the jet potential core end, the flow around the centerline in the region of interest is quite uniform and does not contain turbulence. This observation justifies the coarser rectangular grid used for the centerline region. The rest of the jet core region is discretized using an annular grid, which surrounds the jet core rectangular grid. This grid is called the jet core annular grid. These two grids communicate via high-order overset grid interpolation. An annular jet nozzle lip-line grid discretizes the jet nozzle lip-line region and surrounds the jet core. The rest of the near-nozzle flow region is covered by a side grid, which encloses the jet core grids and the nozzle lip-line grid. The jet core annular grid, jet nozzle lip-line grid, and side grid contain 649 points in the azimuthal direction. We also have an acoustic grid that encloses the side grid. The acoustic grid captures the radiation of the acoustic waves generated in the flow region. The acoustic grid contains fewer grid points in the azimuthal direction. The side grid and the acoustic grid also communicate via high-order interpolation.

Table 1 summarizes the information about the grids used in the simulation. The “grid points” column in the table shows the total number of grid points in every component grid before removing the excess grid overlap. The “unused points” column gives the number of unused points after the excess grid overlap is removed by OGEN, and the “interpolation points” column shows the total number of interpolation points for every grid. The last column shows the number of blocks into which every component block has been partitioned for parallel computing. The governing equations are solved at a total of slightly over 100 million grid points.

The multiblock discretization of the computational mesh on the nozzle surface is shown in Fig. 3. The chevron nozzle has a conical shape. The annular grids that discretize the domain interior and exterior to the nozzle adapt to the shape of the chevrons. Away from the region containing the chevrons, these annular grids become simple cylindrical grids. A cylindrical pipe for which the length is

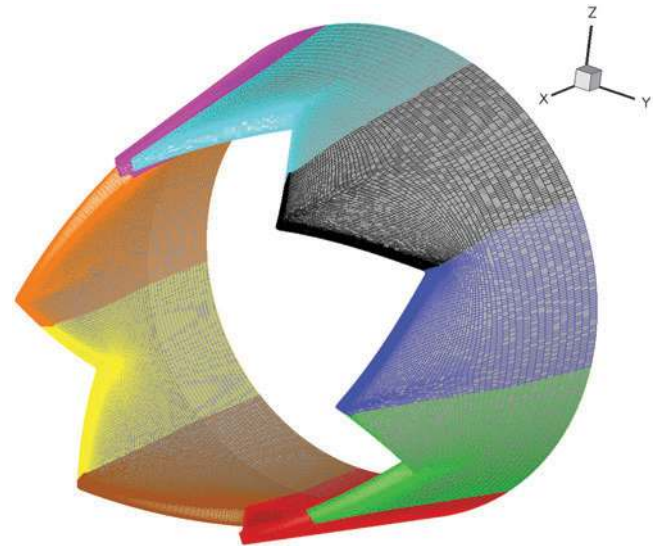


Fig. 3 Multiblock discretization of the SMC001 chevron nozzle surface.

approximately $0.8D_j$ is attached upstream of the chevron nozzle. This cylindrical section is used to generate inflow boundary conditions for the chevron nozzle using the rescaling-recycling procedure described earlier. A boundary-layer thickness of $\delta_{\text{inlet}}/D_j = 3 \times 10^{-2}$ is specified at the cylindrical pipe inlet. The boundary-layer thickness at the cylindrical pipe exit, which coincides with the inlet of the conical chevron nozzle, reaches a value of $\delta_{\text{exit}}/D_j \approx 7 \times 10^{-2}$. The distance between the recycle station and the cylindrical pipe inlet is approximately $13.2\delta_{\text{inlet}}$. The value of the skin friction velocity at the recycle station is $u_\tau/U_j \approx 0.03225$. Based on this skin friction velocity, the constant streamwise grid spacing within the cylindrical pipe corresponds to $\Delta_x^+ \approx 55$, whereas the azimuthal grid spacing on the wall corresponds to $\Delta_\theta^+ \approx 19$. The wall-normal grid spacing in the cylindrical pipe is $\Delta_r^+ \approx 0.74$. The radial grid spacing at the edge of the boundary layer is roughly 10 times the wall-normal grid spacing.

The streamwise wall grid spacing at the inlet of the conical chevron nozzle is equal to the constant streamwise grid spacing within the cylindrical pipe. The streamwise grid spacing on the chevron nozzle wall decreases toward a value of $10^{-3}D_j$ at the chevron edges. In wall units, the streamwise grid spacing at the chevron nozzle exit corresponds to a value of $\Delta_x^+ \approx 3.5$. Because of the contraction of the chevron nozzle, the azimuthal grid spacings on the wall get smaller toward the nozzle exit. Thus, in wall units, $\Delta_\theta^+ < 19$ inside the chevron nozzle. The wall-normal grid spacing on the chevron nozzle wall is roughly the same as that in the cylindrical pipe. However, due to the nozzle contraction, the radial grid spacings in the chevron nozzle boundary layer become finer toward the nozzle exit. At any given location within the cylindrical pipe or the chevron nozzle, the number of radial grid points within the boundary layer ranges from 50 to 60.

The streamwise grid spacing at the nozzle exit is $10^{-3}D_j$ and reaches a value of $0.02D_j$ by $x/D_j = 0.5$. Starting at this location, the streamwise grid spacing in the flow region remains constant at $0.02D_j$ until the start of the sponge zone. The sponge zone attached

Table 1 Grid information

Component grid name	Streamwise points	Radial points	Azimuthal points	Grid points	Unused points	Interpolation points	Number of blocks
Jet core rectangular grid	399	N/A	N/A	1.685775×10^6 ($=399 \times 65 \times 65$)	476, 668	276, 996	7
Jet core annular grid	399	101	649	26.154051×10^6	0	775, 656	126
Jet nozzle lip-line grid	287	42	649	7.823046×10^6	0	0	45
Side grid	343	242	649	53.870894×10^6	0	666, 792	270
Acoustic grid	199	151	425	12.770825×10^6	864, 613	294, 288	64
Total	—	—	—	102.304591×10^6	1.341281×10^6	2.013732×10^6	512

downstream of the physical flow domain contains 40 grid points in the streamwise direction and is $3D_j$ long. The grid is rapidly stretched in this zone. The streamwise grid spacing at the end of the sponge zone is set to $0.25D_j$.

The smallest radial grid spacing on the nozzle exit plane is around $2 \times 10^{-4}D_j$. Chevrons introduce axial vortices, which enhance the mixing of the shear layers. As a result, the width of the mixing layer becomes much larger than that of a round nozzle mixing layer at a given axial location. Thus, a significant number of points in the radial region are needed to cover the enhanced mixing layer region. The radial grid spacing within the lip-line and side grids gradually increase with radial distance. On the nozzle exit plane, the radial grid spacing at the outer edge of the side grid is about $5.4 \times 10^{-3}D_j$. This is the coarsest radial grid resolution on this plane. The radius of the outer edge of the side grid on the nozzle exit plane is approximately one jet nozzle exit diameter. The lip-line and side grids both expand with downstream distance, thus the radial grid spacings also increase with axial distance. The coarsest radial grid spacing, which happens to be at the outer edge of the side grid at the end of the physical domain, is $10^{-2}D_j$. The radius of the outer edge of the side grid at this location is $1.85D_j$.

The acoustic grid enclosing the side grid is fine enough to resolve very high frequencies in the near acoustic field region just outside the shear layers. The radial grid spacing in the vicinity of the FWH control surface, which lies within the acoustic grid, is $\Delta_r/D_j \approx 7.5 \times 10^{-3}$. This gives the estimate of a cutoff Strouhal number of around 37, assuming that the compact scheme we are using needs at least four points per wavelength to accurately resolve an acoustic wave. The number of azimuthal grid points in the acoustic grid is fewer than that in the other three annular grids. The streamwise grid spacing of the acoustic grid is uniform in the physical portion of the domain and is equal to approximately $3 \times 10^{-2}D_j$. The acoustic grid is stretched along the radial direction toward the lateral boundary and also along the streamwise direction within the sponge zone to dissipate the acoustic waves before they reach the boundaries.

Characteristic viscous wall boundary conditions [28] are applied on the nozzle walls. We additionally impose adiabatic boundary conditions on all walls. Although temperature is not one of the solution variables, it is related to density and pressure through the ideal gas relation. Adiabatic wall boundary conditions are enforced by setting the heat flux term in the wall-normal direction to zero in the energy equation. We employ characteristic-type inflow boundary conditions [27] on the inlet of the side grid and the acoustic grid, while Tam and Dong radiation boundary conditions modified by Dong [25] are applied on the lateral boundary of the acoustic grid. We impose characteristic-type outflow boundary conditions [27] at the end of the sponge zone in all grids. The inflow boundary of the cylindrical pipe is taken care of by the inflow generation procedure described earlier.

The flowfield data obtained on the 50-million-point grid were used to initialize the computations on the 100-million-point grid. This led to reduced runtimes on the 100-million-point grid. The simulation on the 100-million-point grid has been run for about 50,000 time steps total. The first 13,000 time steps were used to drive the initial transients out of the domain. The unsteady flow data computed over the next 37,000 time steps were used for the flow statistics, far-field noise calculations via the FWH method, and the two-point velocity correlations within the jet shear layers. The simulation has been performed with implicit time stepping. Three subiterations were applied per time step. The filtering parameter was set to $\alpha_f = 0.47$. The computational time step is $\Delta t = 0.00125D_j/U_j$. With this time step, the data sampling period corresponds to a time scale of $46.25D_j/U_j$ or $51.39D_j/c_\infty$. Using the value of the skin friction velocity at the recycle station $u_\tau/U_j \approx 0.03225$, we see that our time step corresponds to $\Delta t^+ = \Delta t u_\tau^2/\nu_{\text{wall}} \approx 0.14$ in wall units. It is known that the viscous time scale or the Kolmogorov time scale, which is the smallest time scale of turbulence, in a turbulent boundary layer is $\mathcal{O}(1)$ in wall units [34]. Thus, to ensure that the time scales in the nozzle boundary layers are properly resolved, we set our computational time step to be less than the viscous time scale. With this time step, 800 time steps are required for a particle moving at the

jet nozzle exit centerline velocity to travel one nozzle diameter. Also, with the current time step, we see that there are about 53 temporal points in one period of an acoustic wave with a frequency of Strouhal number 15. This Strouhal number corresponds to the cutoff frequency of the experimental measurement with which we will be making a comparison.

A total of 512 processors were used in parallel for the computations on the 100-million-point grid. The simulation was mostly performed on the National Center for Supercomputing Applications Xeon Linux Cluster (Tungsten) (see <http://www.ncsa.uiuc.edu/UserInfo/Resources/Hardware/XeonCluster>). Part of the computation was performed on the Cray XT3 machine (Bigben) at the Pittsburgh Supercomputing Center (see <http://www.psc.edu/machines/cray/xt3/>). About 12 days total runtime is needed on Tungsten for the whole simulation. We should note that the code runs about 18% faster on Bigben. The simulation requires about 150 GB of total memory.

The simulation computes the enhanced shear-layer mixing due to the chevrons in the near-nozzle region in great detail. The state of the mixing layer at a streamwise location $1.5D_j$ downstream of the nozzle exit plane is shown in Fig. 4. It is this enhanced shear-layer mixing that causes the reduction of jet noise at low frequencies and the increase in noise at high frequencies. The time-accurate unsteady flowfield data computed by the LES are provided to the FWH method for far-field noise calculations.

The cylindrical FWH control surface on which certain quantities are integrated for the prediction of far-field noise has an initial radius of about $1.41D_j$ near the inlet boundary of the acoustic grid. The control surface extends to the end of the physical domain. The radius of the surface at this location is equal to approximately $2D_j$. The control surface lies within the acoustic grid and coincides with a grid surface plane on which the radial grid index is held constant. Thus, the unsteady data needed in the surface integrals are directly provided to FWH surface integrals without any need for interpolation. To reiterate, the radial grid spacing in the vicinity of the FWH control surface is $\Delta_r/D_j \approx 7.5 \times 10^{-3}$. This radial grid spacing is about one-tenth of the wavelength of the experimental cutoff frequency (Strouhal number of 15).

The FWH control surface is an open surface, meaning that the inlet and exit planes are not included in the integrals. In a study done on the use of open control surfaces in flow-generated noise applications, Freund et al. [35] indicate that for an open control surface, if the straight line between the source and the observer goes through part of the surface, then the result is acceptable; however, if the line goes through the open part, then the result is erroneous. In this problem, we are only interested in computing the high-frequency noise that

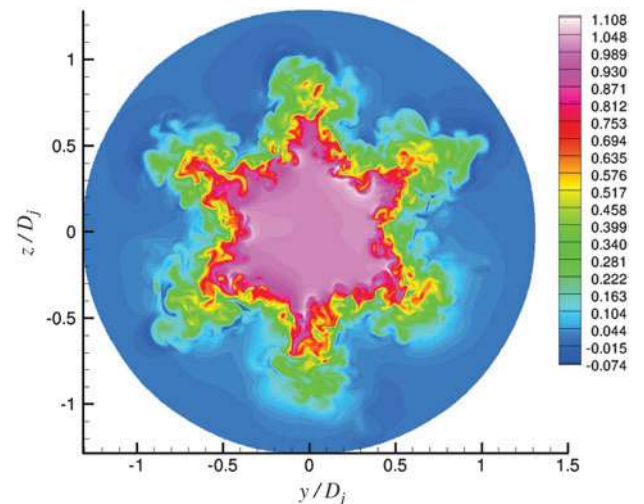


Fig. 4 Instantaneous streamwise velocity contours of the mixing layer at $x/D_j = 1.5$. Nozzle exit plane is at $x/D_j = 0$. Colors denote the magnitude of the instantaneous streamwise velocity normalized by jet centerline velocity at nozzle exit.

propagates in the sideline direction, thus the open FWH control surface we use here captures the noise radiation in this direction with sufficient accuracy. High frequency noise gets generated within the first few nozzle diameters downstream of the nozzle exit and our FWH control surface is long enough to enclose this region.

B. Simulation Results

1. Turbulence Statistics and Mean Flow

We first examine the properties of the boundary layer within the cylindrical pipe attached upstream of the chevron nozzle. To reiterate, this cylindrical pipe is used to generate realistic inflow boundary conditions for the chevron nozzle. The boundary-layer profiles are examined at two locations within the cylindrical pipe. The first location is the recycle station, which is located approximately $0.4D_j$ upstream of the chevron nozzle inlet. The momentum thickness Reynolds number at this station is $Re_\theta \approx 291$. The second location is located downstream of the recycle station and about $0.25D_j$ upstream of the inlet of the chevron nozzle. The conical shape of the chevron nozzle creates a favorable pressure gradient (i.e., pressure decreasing with axial distance) which significantly affects the flow within the last $0.2D_j$ of the cylindrical pipe. Thus, the second station we have chosen to examine approximately represents the last station in the cylindrical pipe that is unaffected by the pressure gradient created by the contraction of the chevron nozzle. The momentum thickness Reynolds number at the second station is $Re_\theta \approx 347$.

Normalized mean streamwise velocity profiles at the two stations are shown in Fig. 5. Here, U^+ and Δr^+ represent the mean streamwise velocity and the normal distance from the nozzle wall, respectively, in wall units. As can be seen in the figure, the profiles agree with the linear equation $U^+ = \Delta r^+$ very well in the viscous sublayer region. The figure also plots the logarithmic layer curve $U^+ = (1/\kappa) \ln(\Delta r^+) + C$, where $\kappa = 0.41$ and $C = 5$. The log layer is defined as the region that lies between the viscous sublayer and the defect layer of a zero-pressure-gradient turbulent boundary layer. We also show Spalart's direct numerical simulation (DNS) data [36] for a zero-pressure-gradient turbulent boundary layer at $Re_\theta = 300$ for comparison. As can be seen in the figure, both of our profiles have a large velocity overshoot above the log law.

The velocity profiles shown here are actually representative of a transitional rather than a fully turbulent boundary layer. In a study done by Rai and Moin [37] on the DNS of transition and turbulence in a spatially evolving boundary layer, the shape of the velocity profile of the boundary layer at various stages during transition from laminar

to turbulent state was clearly demonstrated. They have shown that a boundary layer in the transitional stage clearly has a large overshoot above the log law, similar to what is observed here. Thus, the velocity profiles shown here are quite similar to those of transitional boundary layers in the study of Rai and Moin [37].

This implies that the cylindrical pipe is feeding transitional rather than fully turbulent boundary layers into the chevron nozzle. The fact that we are unable to obtain fully turbulent boundary layers indicates that there are some issues with the inflow generation method we have implemented. Although the inflow generation method of Lund et al. [11] has been successfully used to generate inflow conditions for boundary layers with Re_θ of at least 1500, the Re_θ values of our pipe flow boundary layers are much lower. Thus, the relatively low Re_θ of our boundary layers could be another suspect. We have also attempted to use another simpler recycling technique developed by Spalart et al. [38]. However, with this simplified method, our pipe flow was observed to become laminar after a few hundred inertial times (δ_{inlet}/U_{pipe} , where U_{pipe} is the pipe core velocity). This is believed to be related to how the pipe flow was initialized. A search for a satisfactory inflow generation technique that will generate fully turbulent boundary layers for the Re_θ values we can currently afford is still ongoing.

The axial, radial, and azimuthal turbulence intensities at the two stations within the cylindrical pipe are shown in Fig. 6. The intensities are normalized by the wall friction velocity u_τ . The DNS profiles from Spalart's turbulent boundary-layer calculations [36] at $Re_\theta = 300$ are also shown in the same figure for comparison. Our profiles have good overall qualitative agreement with the corresponding DNS profiles. It is observed that the peak axial turbulence intensity at the two stations is greater than the DNS value, whereas the other two peak turbulence intensities are lower than the corresponding DNS values. This is mostly likely related to our inflow generation method. The method seems to be generating too much axial intensity and too little radial intensity. Our axial turbulence intensity peaks very near the wall at both stations, where $\Delta r^+ \approx 17$. The azimuthal intensity reaches its peak value at $\Delta r^+ \approx 25$ –30, whereas the radial turbulence intensity reaches its peak value at $\Delta r^+ \approx 65$.

The boundary-layer turbulence intensity and mean axial velocity profiles at the inlet of the chevron nozzle are shown in Fig. 7. Here, the mean axial velocity and turbulence intensities are normalized by U_j . The peak axial intensity is about $0.123U_j$, whereas the peak azimuthal and radial intensities are about $0.03U_j$ and $0.02U_j$, respectively. The peak axial intensity at the chevron nozzle inlet is much larger than the other two components.

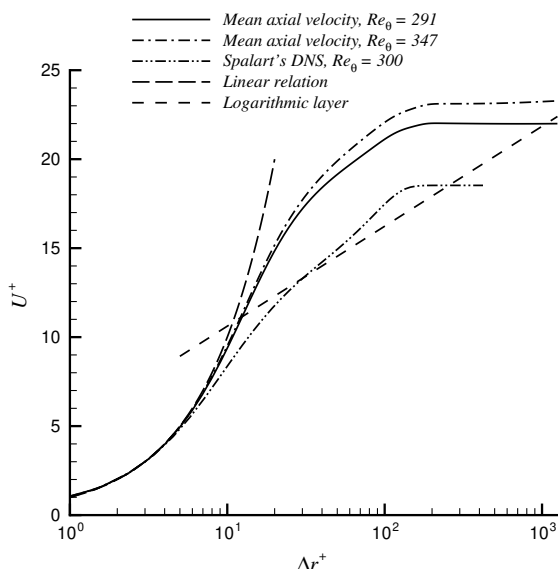


Fig. 5 Cylindrical pipe flow mean axial velocity profiles (in wall units) and comparison with Spalart's DNS at $Re_\theta = 300$ [36].

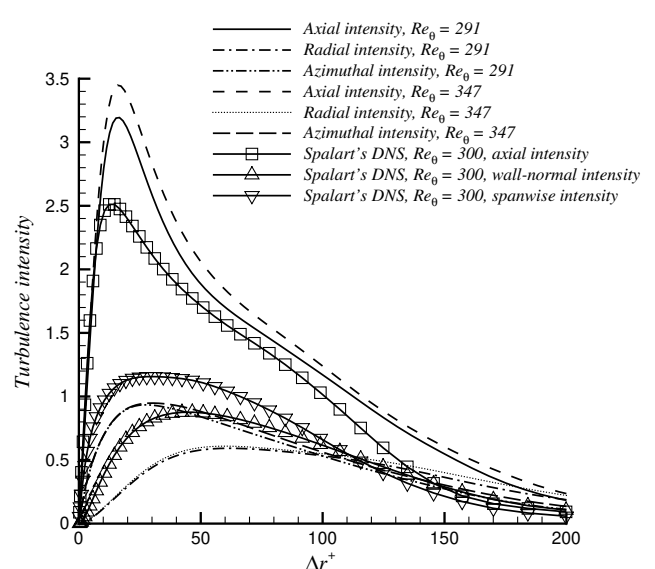


Fig. 6 Cylindrical pipe flow turbulence intensity profiles (in wall units) and comparison with Spalart's DNS at $Re_\theta = 300$ [36].

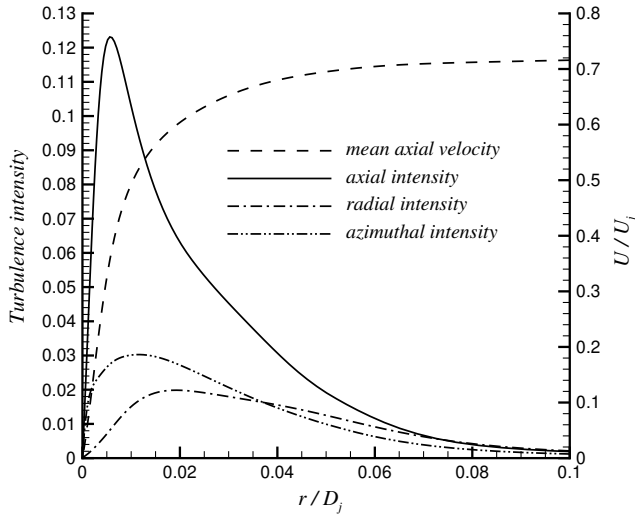


Fig. 7 Mean axial velocity and normalized turbulence intensity profiles at the inlet of the chevron nozzle.

Next, we look at the flow development downstream of the nozzle exit plane. We first examine the axial variation of the mixing layer thicknesses. As is obvious from Fig. 4, the mixing layer thickness varies greatly in the azimuthal direction. Thus, we can compute a minimum and a maximum shear-layer thickness at every axial location. The axial variation of the minimum and maximum shear-layer thickness is shown in Fig. 8. We also plot the ratio of the maximum to minimum thickness. Immediately downstream of the nozzle exit plane, the minimum shear-layer thickness is about $0.0066D_j$, whereas the maximum shear-layer thickness is about $0.115D_j$. The initial value of the shear-layer thickness ratio is around 17.5 and decays rapidly within the first half of a diameter downstream of the nozzle exit. The thickness ratio continues to decrease slowly for the next 3 diameters. As expected, the shear-layer thicknesses increase with axial distance.

The oscillations in the shear-layer thickness growth curves are due to the limited statistical sample size. A larger sample size would help smooth these curves. It appears that the maximum shear-layer thickness initially displays a linear growth at a certain rate until about $x/D_j \approx 1.2$. The growth downstream of $x/D_j \approx 1.5$ also appears almost linear, yet the growth rate (line slope) seems to be a bit reduced compared with the initial region. The minimum shear-layer thickness curve displays an almost linear growth starting at a short distance downstream of the nozzle exit and continuing until about

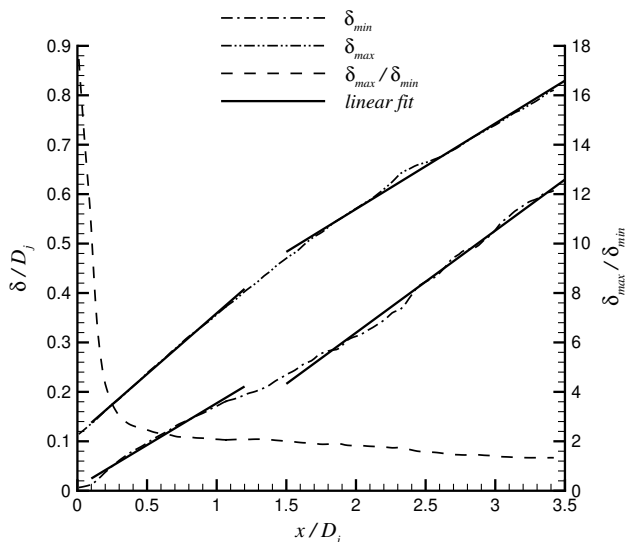


Fig. 8 Streamwise variation of minimum and maximum shear-layer thicknesses.

$x/D_j \approx 1-1.2$. Downstream of $x/D_j \approx 1.5$, we again see an almost linear growth, yet, this time, the rate of growth has increased relative to the initial region. The region in between $x/D_j \approx 1-1.2$ and $x/D_j \approx 1.5$ appears to be a transition region where the shear layers are adjusting their growth rates.

The axial variation of the three components of the peak turbulence intensity and the comparison with experimental measurements [1] are depicted in Fig. 9. The oscillations in the LES curves are due to the limited statistical sample size. Because we have six symmetric chevrons, the data on every axial plane are first averaged over 12 slices. This is done for both the LES and the experimental data. The peak turbulence intensities are then extracted from the averaged data. The turbulence intensities are normalized by the jet nozzle exit centerline velocity U_j . As can be seen in the plot, the LES turbulence intensities reach their peak at a short distance downstream of the nozzle exit. The experimental data, on the other hand, show a very different trend in the first diameter downstream of the nozzle exit, the experimental data on the first four particle image velocimetry (PIV) planes, which are located within the first diameter of the nozzle exit, are rather questionable.

It should also be noted here that the level of the discrepancy observed between the experimental and LES peak axial intensity is not the same as the discrepancy levels observed for the other two components. The discrepancy level observed for the peak radial and azimuthal intensities are greater than that observed for the peak axial intensity. The nozzle inlet conditions in the simulation could be responsible for this. It was shown earlier that, compared with Spalart's DNS of a flat-plate boundary layer [36], the inflow forcing used in this study puts too much energy into the axial velocity fluctuations in the boundary layers and too little energy into the radial and azimuthal components. Such a distribution of the turbulent kinetic energy within the nozzle boundary layers could be responsible for the different levels of the discrepancies observed between the LES and the experiment in the near-nozzle region. Unfortunately, no nozzle boundary-layer measurements were made in the experiment. Thus, it is not possible to compare the LES nozzle inlet conditions with the inlet conditions of the experiment.

Going back to the comparison between the LES and the experiment, we see that, on the fifth PIV plane, which is located at $x/D_j = 1.878$, the LES peak axial intensity is about 17.4% lower than the experimental value, whereas the LES peak radial intensity is 17.3% larger than the experimental value and the LES peak azimuthal intensity is 15.2% larger than the experimental value. On the sixth PIV plane, located at $x/D_j = 3.287$, the LES peak axial intensity is about 15.8% lower than the experimental value, whereas the LES

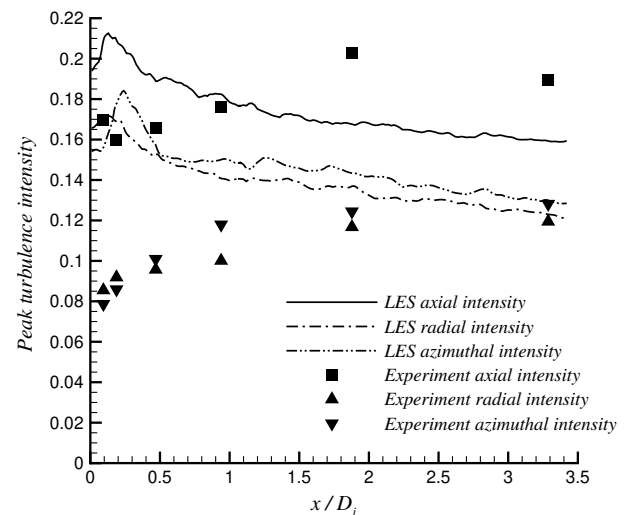


Fig. 9 Streamwise variation of peak axial, radial, and azimuthal turbulence intensities.

peak radial intensity and the LES peak azimuthal intensity are very close to the corresponding experimental values. In the following section, we will make a side-by-side comparison of the LES results and experimental measurements on some of the PIV planes.

2. Comparison of Time-Averaged Quantities with Experimental Data

In this section, we will make a comparison of the LES results with the experimental measurements on several PIV planes in the near-nozzle region. The axial location of the comparison planes are $x/D_j = 0.0939$, 1.878, and 3.287, respectively. There are three more PIV planes at $x/D_j = 0.1878$, 0.4695, and 0.939. However, we will skip the comparisons on these planes for the sake of brevity. Although there are additional PIV planes located farther downstream, there are no LES data in that region due to limited streamwise domain size. Because we have six symmetric chevrons, the data on every axial plane are averaged over 12 slices. This is done for both the LES and the experimental data. The comparisons will be made using the averaged data.

We will compare the normalized mean axial velocity contours and the three components of the normalized turbulence intensity. The jet nozzle exit centerline velocity U_j is used to nondimensionalize the data presented here. The normalized axial, radial, and azimuthal turbulence intensities are defined as $\sqrt{\langle u'u' \rangle}/U_j$, $\sqrt{\langle v_r v_r' \rangle}/U_j$, and $\sqrt{\langle v_\theta v_\theta' \rangle}/U_j$, respectively. Here, $\langle \rangle$ is the time averaging operator and the superscript $'$ denotes the fluctuation from mean value. Moreover, u is the axial velocity component, whereas v_r and v_θ are the radial and azimuthal velocity components, respectively, which are easily computed using a coordinate transformation from Cartesian to cylindrical coordinates. In the slice-comparison figures that will be shown shortly, the $y/D_j = 0$ plane coincides with the plane which is shared by two neighboring chevrons at their root. This is also called the chevron valley plane.

The normalized mean axial velocity contours on the PIV planes are compared in Figs. 10–12. On the first PIV plane shown in Fig. 10, we see significant differences between the LES and the experiment. Because of the errors in the measurement method, the experiment appears to have an almost uniform shear-layer thickness on this plane. As also acknowledged by experimentalists, the relatively thin shear layers in the very near-nozzle region make accurate PIV measurements in this region quite difficult. The LES, on the other hand, clearly shows the dramatic difference between the minimum and maximum shear-layer thicknesses on this first PIV plane. Although not shown here, the comparisons on the PIV planes at $x/D_j = 0.1878$ and 0.4695 display the same issue with the experimental data. Looking at the comparison on the PIV plane at $x/D_j = 0.939$, not shown here, and the remaining two PIV planes shown in Figs. 11 and 12, we observe good overall similarity between the experimental and LES shear layers. However, the LES shear

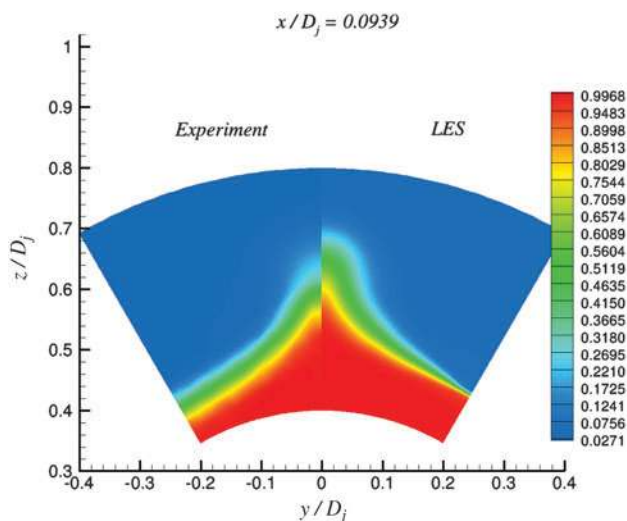


Fig. 10 Comparison of mean axial velocity contours at $x/D_j = 0.0939$.

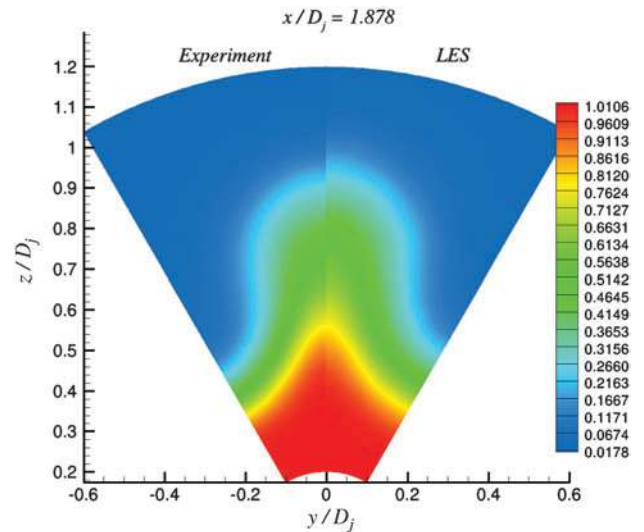


Fig. 11 Comparison of mean axial velocity contours at $x/D_j = 1.878$.

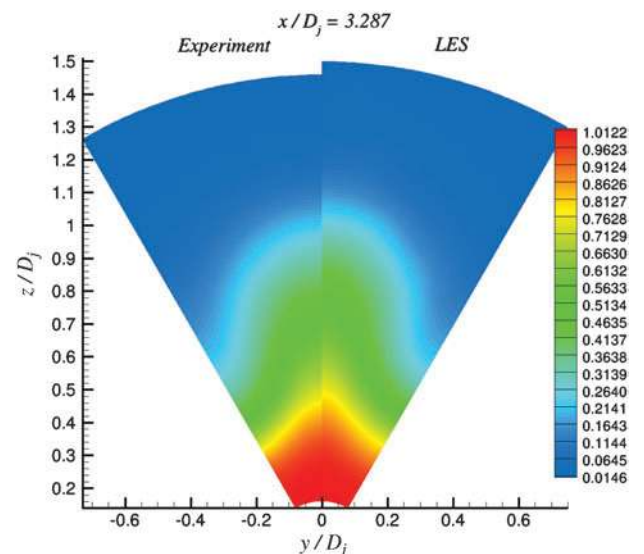


Fig. 12 Comparison of mean axial velocity contours at $x/D_j = 3.287$.

layer is seen to be a bit thicker than the experiment on these PIV planes. This is likely due to initial condition effects and the Reynolds number difference.

The radial distributions of the mean axial velocity at the azimuthal locations corresponding to the chevron tip and valley planes on two PIV locations are shown in Fig. 13. These are the PIV planes located at $x/D_j = 0.939$ and 3.287. The right-side edge of the LES slice or the left-side edge of the experimental slice shown in Fig. 10 corresponds to the chevron tip plane, whereas the left-side edge of the LES slice or the right-side edge of the experimental slice corresponds to the chevron valley plane. Reasonable agreement between the computation and the experiment is observed in these profile comparisons.

The normalized axial turbulence intensity contours on the PIV planes are compared in Figs. 14–16. The comparison on the first PIV plane shown in Fig. 14 depicts significant differences between the LES and the experiment. The LES peak axial intensity is clearly higher than the experimental value on this plane. The comparisons on the PIV planes at $x/D_j = 0.1878$ and 0.4695, not shown here, depict a similar trend. On the PIV plane at $x/D_j = 0.939$, not shown here, we start to see some similarity between the LES and the experiment, but there are still important differences. The best agreement between the LES and the experiment is observed on the last two PIV planes shown in Figs. 15 and 16. On these two planes, the experimental peak

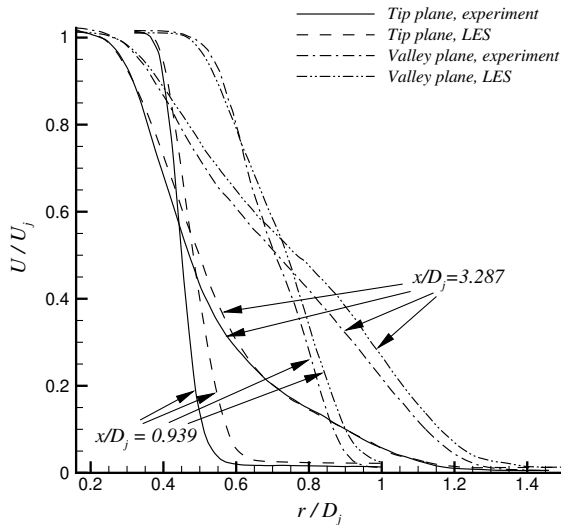


Fig. 13 Radial profiles of mean axial velocity at azimuthal positions corresponding to chevron tip and valley planes.

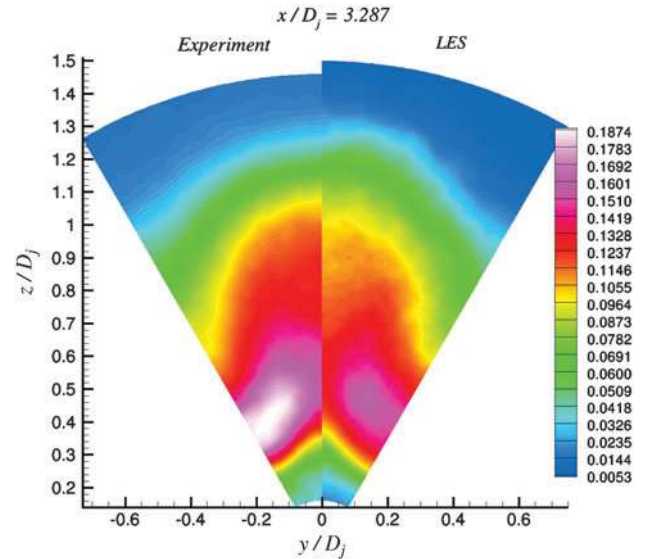


Fig. 16 Comparison of axial turbulence intensity contours at $x/D_j = 3.287$.

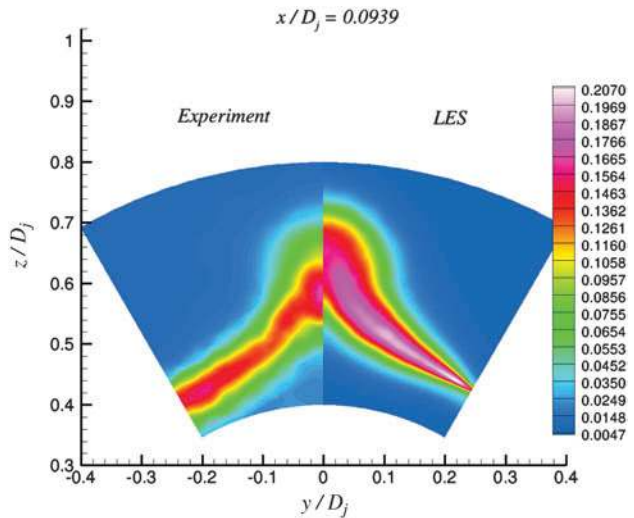


Fig. 14 Comparison of axial turbulence intensity contours at $x/D_j = 0.0939$.

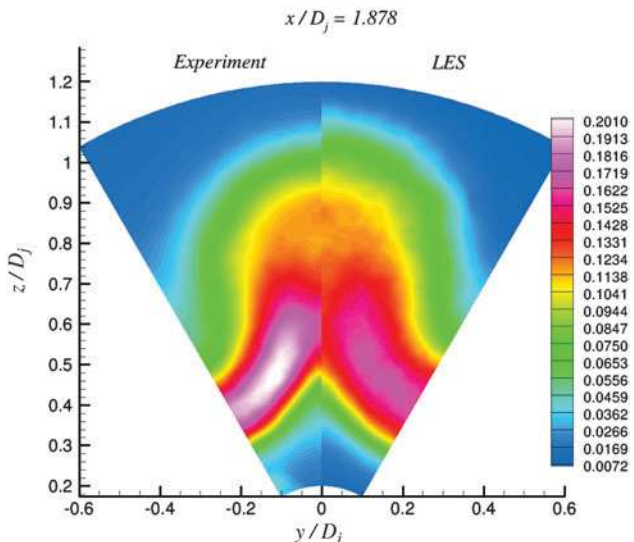


Fig. 15 Comparison of axial turbulence intensity contours at $x/D_j = 1.878$.

axial intensity is higher than the LES. The radial distributions of the axial turbulence intensity at the chevron tip and valley plane azimuthal locations on two PIV planes are depicted in Fig. 17. Looking at these comparisons, we observe significant differences between the profiles taken at $x/D_j = 0.939$, although there is better agreement observed between the profiles taken at $x/D_j = 3.287$.

The normalized radial turbulence intensity contours on the PIV planes are compared in Figs. 18–20. Once again, we observe significant differences in the radial intensity comparisons on the first three PIV planes, of which only the first one is shown in Fig. 18. The experimental radial intensities on these first three planes are significantly lower than the LES. The significant difference between the LES and the experiment is still visible on the PIV plane at $x/D_j = 0.939$, which is not shown here. The best agreement between the LES and experiment is again seen on the last two PIV planes shown in Figs. 19 and 20. The peak LES radial intensity on the last PIV plane is almost the same as that in the experiment. The radial distributions of the radial turbulence intensity at the chevron tip and valley plane azimuthal locations on two PIV planes are shown in Fig. 21. Again, the differences between the profiles are quite significant at $x/D_j = 0.939$, although the agreement between them is better at $x/D_j = 3.287$.

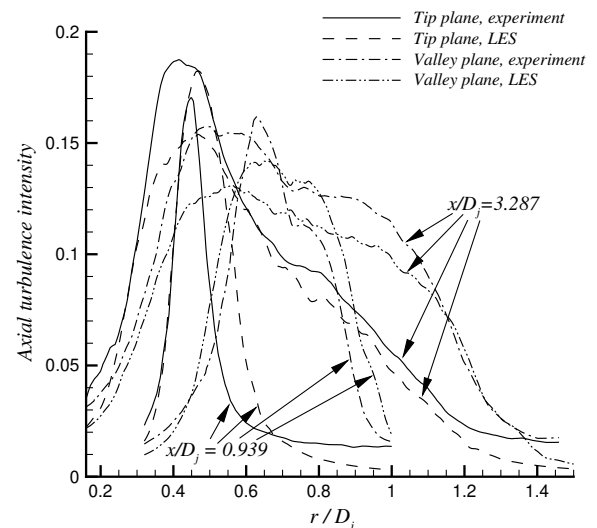


Fig. 17 Radial profiles of axial turbulence intensity at azimuthal positions corresponding to chevron tip and valley planes.

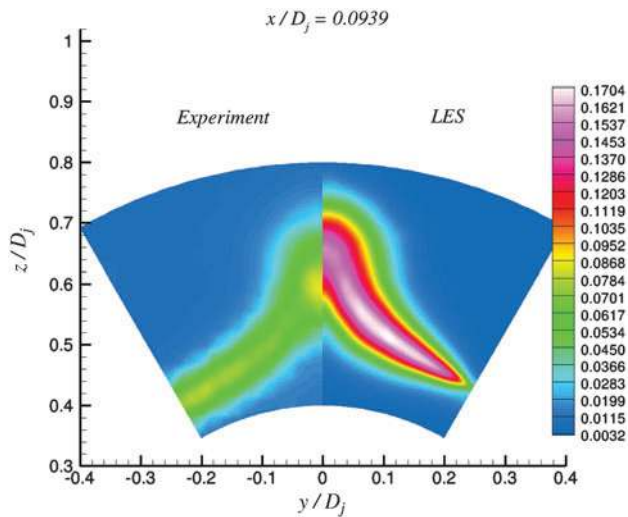


Fig. 18 Comparison of radial turbulence intensity contours at $x/D_j = 0.0939$.

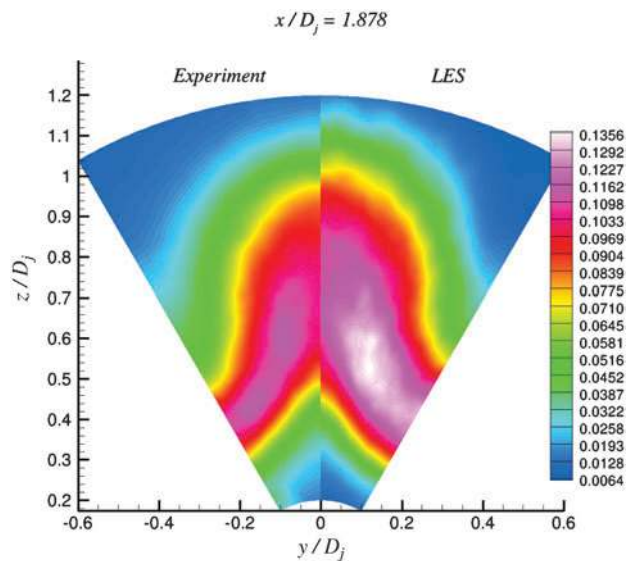


Fig. 19 Comparison of radial turbulence intensity contours at $x/D_j = 1.878$.

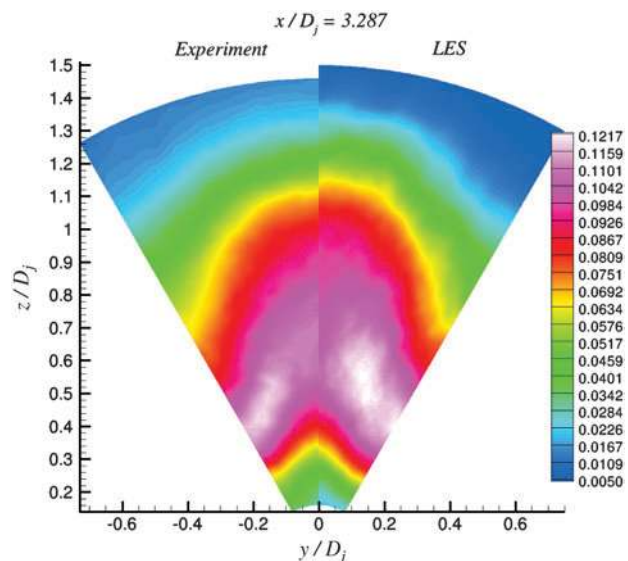


Fig. 20 Comparison of radial turbulence intensity contours at $x/D_j = 3.287$.

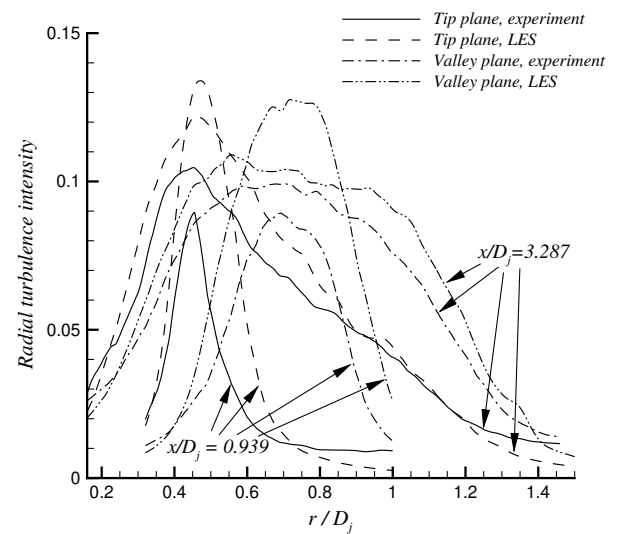


Fig. 21 Radial profiles of radial turbulence intensity at azimuthal positions corresponding to chevron tip and valley planes.

Finally, the normalized azimuthal turbulence intensity contours on the PIV planes are compared in Figs. 22–24. Once again, we observe significant differences between the LES and the experiment on the first few PIV planes closest to the nozzle exit and the best agreement is observed on the last two PIV planes. The peak LES azimuthal intensity on the last PIV plane is almost the same as that in the experiment. The radial profiles of the azimuthal turbulence intensity at the chevron tip and valley plane azimuthal locations on two PIV planes are plotted in Fig. 25. The significant differences at $x/D_j = 0.939$ are once again clearly visible, and there is better agreement observed at $x/D_j = 3.287$.

In summary, the LES and experimental turbulence intensities compare quite well on the last two PIV planes. Some differences on these two planes are not surprising at all because the initial condition effects and the Reynolds number difference are expected to play a role in the development of the mixing layers in the near-nozzle region. The uncertainties in the experimental measurements have to be kept in mind as well. Some of the discrepancies observed in the comparison of turbulence intensities on the first few PIV planes closest to the nozzle exit are likely due to the poor quality of the experimental measurements in the first diameter downstream of the nozzle exit.

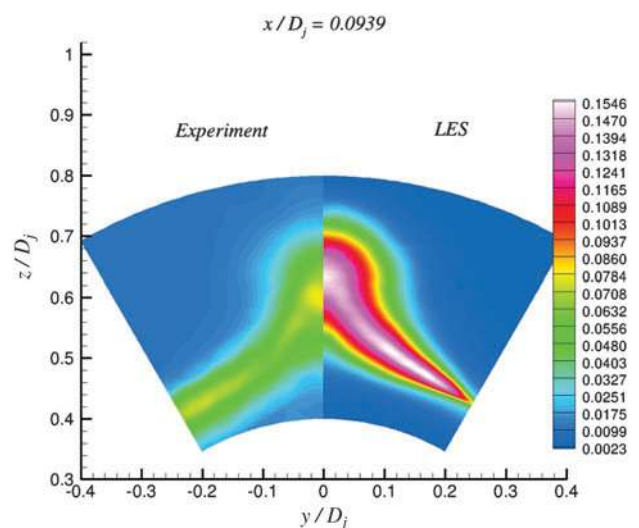


Fig. 22 Comparison of azimuthal turbulence intensity contours at $x/D_j = 0.0939$.

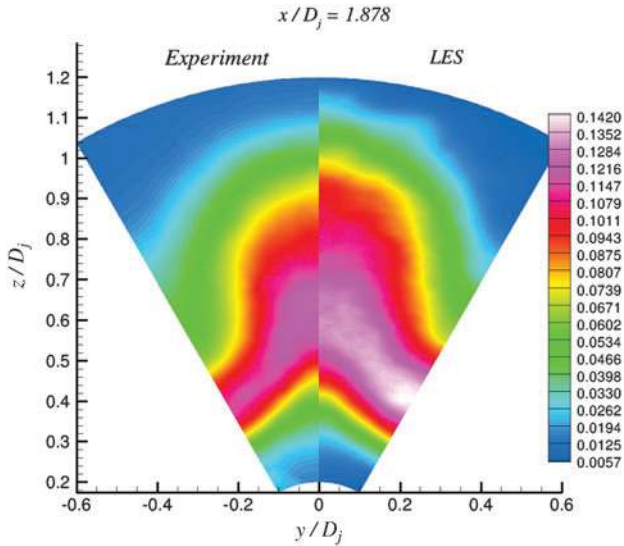


Fig. 23 Comparison of azimuthal turbulence intensity contours at $x/D_j = 1.878$.

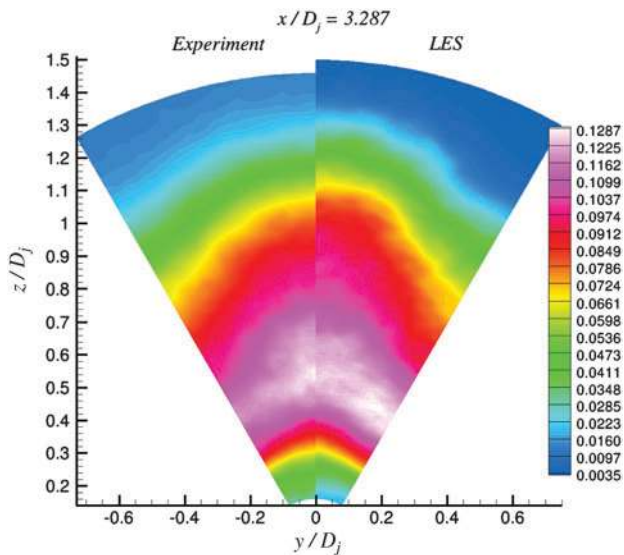


Fig. 24 Comparison of azimuthal turbulence intensity contours at $x/D_j = 3.287$.

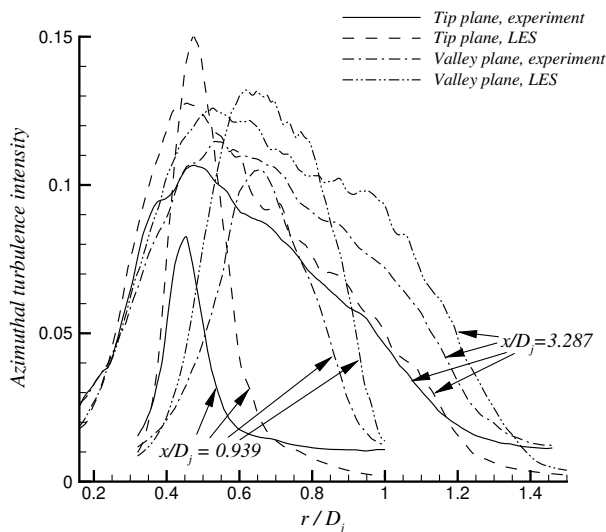


Fig. 25 Radial profiles of azimuthal turbulence intensity at azimuthal positions corresponding to chevron tip and valley planes.

3. Jet Acoustics

It is well-known that the high-frequency noise is most dominant in the sideline direction. Thus, we next show a comparison of the LES and the experimental noise spectrum [1] in this direction. The one-third octave spectrum computed by the LES and its comparison with the experiment at the 90-deg (measured from the jet axis) observation location is shown in Fig. 26. LES acoustics results obtained using both the 50-million- and 100-million-point grids are shown in this figure. Narrowband spectrum from the 100-million-point calculation is also included in the same figure. The observation location is $6D_j$ away from the jet nozzle exit centerline. In the simulations, far-field acoustic pressure signals were computed using the FWH method at 24 observer points that are uniformly distributed on a circle for which the radius is equal to $50D_j$. The center of the circle is the same as the jet centerline at nozzle exit. The noise spectra computed at these 24 observer points were averaged to get the final averaged spectrum in the sideline direction. This averaged spectrum was then adjusted for the observation location at $6D_j$ away from the jet nozzle exit centerline using the R^{-1} decay rule, which assumes that the root mean square of the acoustic pressure is inversely proportional to the distance from the source. In the scaling, the source point is taken as the jet nozzle exit centerline point. The experimental noise measurements were taken in the far field and were adjusted to the observer location at $6D_j$ using the same procedure.

One should keep the following issues in mind when comparing the LES prediction with the experiment:

- 1) The experimental Reynolds number is about 14 times the LES Reynolds number.
- 2) Although the experimental Reynolds number is high enough to ensure fully turbulent boundary layers inside the experimental nozzle, the peak turbulence intensities in the experimental nozzle boundary layers are unknown, thus creating uncertainties.
- 3) The state of the boundary layer entering the chevron nozzle in the LES is transitional.
- 4) The low-frequency part of the spectrum is missing in the LES because those frequencies are mostly generated in the further downstream region, which is not included in the current LES due to computational limitations.

Despite these issues, the spectra comparison looks very encouraging. Let us focus on the LES acoustics results obtained using 100 million grid points first. As can be seen in the plot, starting at around Strouhal number 1.1, the LES sound pressure level (SPL) values are in very good agreement with the experiment up to a Strouhal number of about 5.3. The LES clearly captures the peak region of the spectrum accurately. For greater Strouhal numbers, the SPL difference becomes larger. Up until a Strouhal number of about

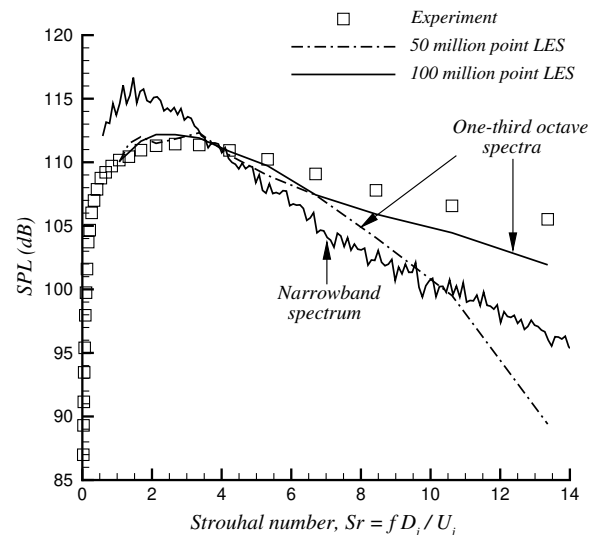


Fig. 26 Comparison of one-third octave noise spectra for the 90-deg observation location. Narrowband spectrum from the 100-million-point calculation is also shown.

10.6, the biggest difference is about 2 dB. The difference becomes about 3.5 dB at the highest frequency. The SPL differences in the very high Strouhal number range are perhaps partially due to the lower Reynolds number of the computation. They may also be related to initial condition differences mentioned earlier.

It would be interesting to see if there would be any difference in the predicted noise spectrum if we could manage to feed fully turbulent rather than transitional boundary layers into the chevron nozzle. Further grid refinement might affect the predictions in the high-frequency range as well, but this remains to be shown via simulations on even finer grids, which would require significant computing resources. Another source for the difference could be the possibility of some rig noise in the experiment, which might make the SPL values in the high-frequency range higher than what they should be. In the figure, we also show results from the preliminary computation, which was performed using 50 million grid points. As can be seen in the figure, in the high-frequency range, there is a large difference between the LES results obtained on the two grids. The coarser grid is clearly insufficient to accurately capture the high frequencies.

When adjusted from model scale to jet engine scale, the high frequencies, which are most dominant in the sideline direction, translate into the frequencies that are most annoying to the human ear. Accurate prediction of the sideline noise spectrum is therefore important for this reason. The sideline noise spectrum is clearly one of the criteria in determining whether a particular nozzle design is successful or not. Although the current computation cannot predict the noise directivity because of the limited streamwise domain size, it can predict the sideline noise spectrum quite satisfactorily.

The present work models the nozzle geometry explicitly in the computation and attempts to generate as realistic nozzle inlet conditions as possible using a rescaling-recycling technique. However, the deficiencies of our recycling method discussed earlier and the Reynolds number difference between the simulation and the experiment mean that the initial momentum thickness of the jet shear layer in the computation certainly does not match that of the experiment. The experimental nozzle boundary-layer turbulence intensities are also unknown, and this adds even more uncertainty. Nevertheless, the good level of agreement in the acoustics predictions seems to imply that exactly matching the initial momentum thickness of the shear layer and the initial shear-layer turbulence intensity levels is perhaps not that critical. As shown earlier, the transitional boundary layers entering the chevron nozzle in the present work possess turbulence intensity profiles that have good qualitative agreement with those of a fully turbulent flat-plate boundary layer, although the peak turbulence intensity levels are not matched exactly. Moreover, chevrons introduce axial vorticity into the jet shear layers and because of the stirring effect of the axial vortices, the turbulence seems to become fully developed quite quickly for the chevron nozzle flows. It is possible that these flows may be less sensitive to details of the turbulence in the initial boundary layers. On the other hand, the very high-frequency end of the spectrum is likely to depend on the properties of the initial nozzle wall boundary layer and the developing mixing layer close to the nozzle exit, and this might explain the 3.5 dB difference seen within the very high-frequency region. Nevertheless, considering the fact that the experimental uncertainty can be 2 or 3 dB, the observed 3.5 dB difference is still quite reasonable.

We should also note here that, in the present study, the streamwise extent of the domain is 3.75 diameters downstream of the nozzle exit. Thus, the domain is not long enough to contain the jet potential core end region. The truncation of the computational domain before the jet potential core end means that the noise generated near and downstream of the jet potential core end is missing in the present computation. According to the experimental study of Narayanan et al. [39], which was conducted to identify noise source locations in round jets, this missing region can have a significant contribution for Strouhal frequencies of up to about two for a round jet. Yet, despite the short streamwise domain size, the spectra predicted by the LES in the present work turn out to be quite good down to about a Strouhal frequency of about one. Thus, it may be argued that, even though there is good agreement observed in the low-frequency region, this

could be due to some kind of error cancellation. However, this is speculation at this point and needs to be verified through further analysis. Hence, the low-frequency part of the LES spectra in the present work should be looked upon with some caution.

A good topic for future work would be to further extend the domain in the streamwise direction and repeat the computation on the new domain. This would be very useful for seeing the effect of the longer domain on the low-frequency part of the noise spectra. We estimate that extension of the domain to 10 diameters downstream of the nozzle exit would require about 175–200 million grid points total. This estimation assumes that the azimuthal grid resolution in the region downstream of the jet potential core end is roughly twice as coarse as that in the near-nozzle region. As the length scales get larger with axial distance, coarsening the mesh in the azimuthal direction downstream of the jet potential core is not expected to have a significant negative impact. Of course, it is possible to keep the same azimuthal resolution everywhere, but this would double the number of points needed in the downstream region. The axial and radial grid spacings in the downstream region are assumed to be similar to those found in the near-nozzle region. A simulation on 175–200 million grid points would require about 900–1000 processors and is certainly possible to do on present day supercomputers. This new simulation would need to be run longer than the simulation on the shorter domain, as the streamwise travel distance the jet flow has to cover would be larger. We estimate that the simulation would take about one month of runtime on present day supercomputers to cover a time scale of about $200D_j/U_j$.

4. Length and Time Scales in the Mixing Layer

To estimate the length scales in the middle of the mixing layer, where $U/U_j = 0.5$, we can make use of two-point velocity correlations. We estimate the turbulent length scale in a particular direction by the 50% correlation distance of the velocity component in that direction. For example, let us consider the two-point correlation of the radial velocity component in the radial direction, which is defined as follows

$$\mathcal{R}_{rr}(r_o, \xi, t) = \frac{\langle v'_r(r_o, t)v'_r(r_o + \xi, t) \rangle}{\langle v'_r(r_o, t)v'_r(r_o, t) \rangle} \quad (14)$$

where r_o is the radial location and ξ represents the spatial separation between the two points. Now, if

$$\langle v'_r(r_o - r_{\text{left}}, t)v'_r(r_o, t) \rangle = 0.5 \langle v'_r(r_o, t)v'_r(r_o, t) \rangle \quad (15)$$

and

$$\langle v'_r(r_o + r_{\text{right}}, t)v'_r(r_o, t) \rangle = 0.5 \langle v'_r(r_o, t)v'_r(r_o, t) \rangle \quad (16)$$

then the local 50% correlation radial length scale is defined as $L(r_o) = r_{\text{left}} + r_{\text{right}}$, where r_{left} and r_{right} are the distances from the correlation peak to the left and right 50% correlation points. On the other hand, the radial velocity scale associated with this length scale can be taken as the local radial turbulence intensity. Thus, to estimate the corresponding time scale in the radial direction $\tau(r_o)$, we can simply use the relation $\tau(r_o) = L(r_o)/v'_r(r_o)$ [where $v'_r(r_o)$ is the local radial turbulence intensity] from dimensional analysis. Similar relations can be defined to estimate the length and time scales in other coordinate directions.

In a round jet mixing layer, the azimuthal direction is the statistically homogenous direction. In such a mixing layer, the mean axial velocity at a given radial location is constant along the azimuthal direction. On the other hand, for a chevron jet mixing layer, the mean axial velocity at a given radial location is no longer constant along the azimuthal direction. Thus, we now define a new coordinate direction to be called λ , along which the mean axial velocity remains constant. This is a more natural choice for the chevron jet mixing layer. Hence, the λ direction in the chevron jet mixing layer is analogous to the azimuthal direction in the round jet mixing layer. However, the chevron jet mixing layer is not statistically homogeneous along the λ direction. Instead, it is periodic in that direction.

Next, we will take a look at some two-point velocity correlations along the radial and the λ direction at several locations downstream of the nozzle exit. These correlations are taken at the half-velocity point in the shear layer. To compute these correlations, one first needs the Cartesian velocity components at the correlation points, which do not necessarily coincide with the LES grid points. Thus, interpolation is necessary to obtain the velocities. The Cartesian velocity components then need to be converted to the radial velocity component v_r and the λ direction velocity component v_λ . Conversion to v_r is quite trivial. On the other hand, to obtain v_λ , one has to take the dot product of the local Cartesian velocity vector with the local unit vector in the λ direction. Using the mean axial velocity data on a given axial plane, we can easily extract the λ direction curve along which the mean axial velocity remains constant at the desired value (for example, $U/U_j = 0.5$ at the half-velocity point). We can then compute the local unit vectors in the λ direction using the information about the extracted λ direction curve.

The correlations along the radial direction at the half-velocity point in the minimum and maximum shear-layer thickness locations on three axial planes are plotted in Figs. 27 and 28. Similarly, the correlations along the λ direction at the half-velocity point in the minimum and maximum shear-layer thickness locations on the

same three planes are plotted in Figs. 29 and 30. As can be seen in the figures, the correlations become wider with increasing downstream distance, implying that the length scales are becoming larger with axial distance. This is expected for a mixing layer.

The azimuthal variation of the radial and λ direction 50% correlation lengths along the half-velocity curve are plotted in Fig. 31. In this figure, on a given axial plane, $\theta = 60$ deg corresponds to the edge of the slice where the shear-layer thickness is a minimum, whereas $\theta = 90$ deg corresponds to the edge of the slice where the shear-layer thickness is a maximum. (For example, see Figs. 10–12 for the azimuthal variation of shear-layer thickness at a given axial location.) As can be seen in the figure, the length scales within the thin shear-layer side are smaller than they are in the thick shear-layer side, although the difference in the size of the length scales is not much on the third axial plane. The length scales get bigger with axial distance, as expected. An interesting observation is the fact that the radial and λ direction length scales in the middle of the mixing layer on a given axial plane are comparable to each other.

To make matters more interesting, in Fig. 32, we plot the azimuthal variation of the radial and λ direction eddy turnover frequencies along the half-velocity curve. The eddy turnover frequencies are computed using the inverse of the corresponding time scales in the

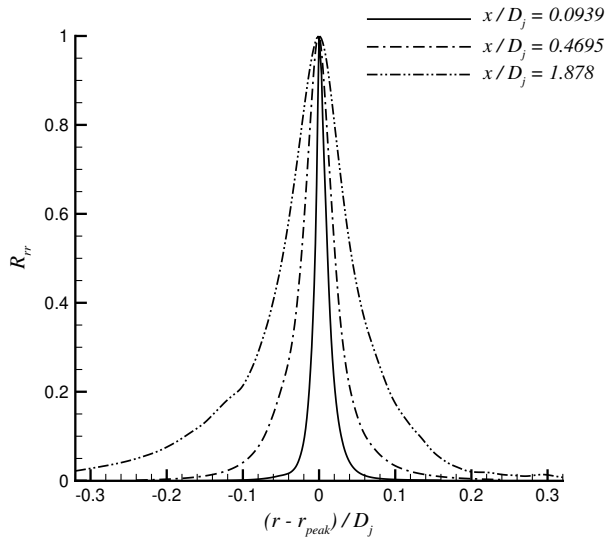


Fig. 27 Two-point correlations of the radial velocity R_{rr} at the half-velocity point in the minimum shear-layer thickness location.

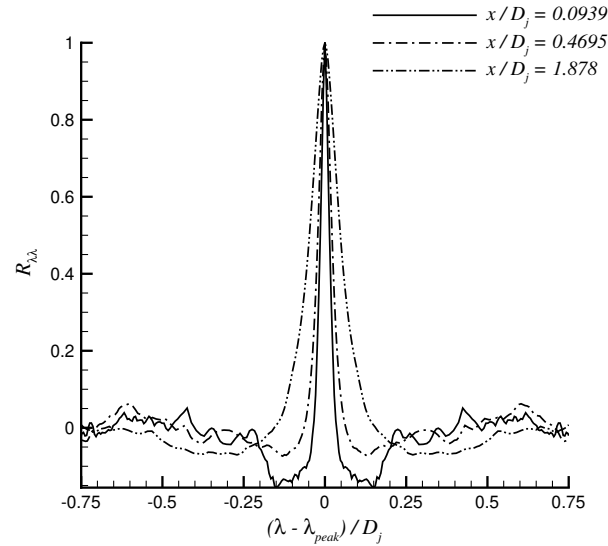


Fig. 29 Two-point correlations of the λ direction velocity $R_{\lambda\lambda}$ at the half-velocity point in the minimum shear-layer thickness location.

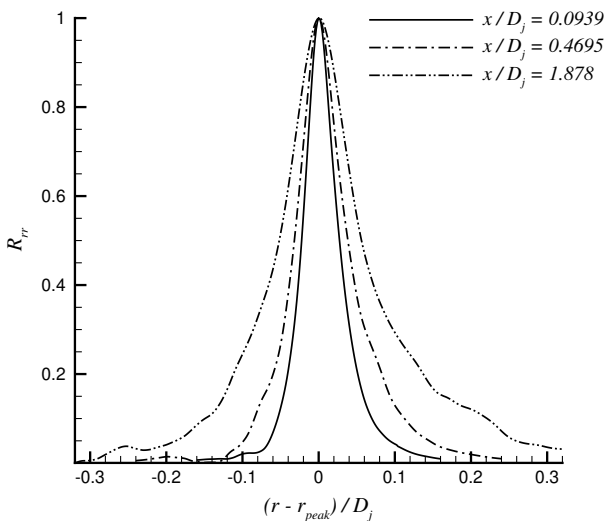


Fig. 28 Two-point correlations of the radial velocity R_{rr} at the half-velocity point in the maximum shear-layer thickness location.

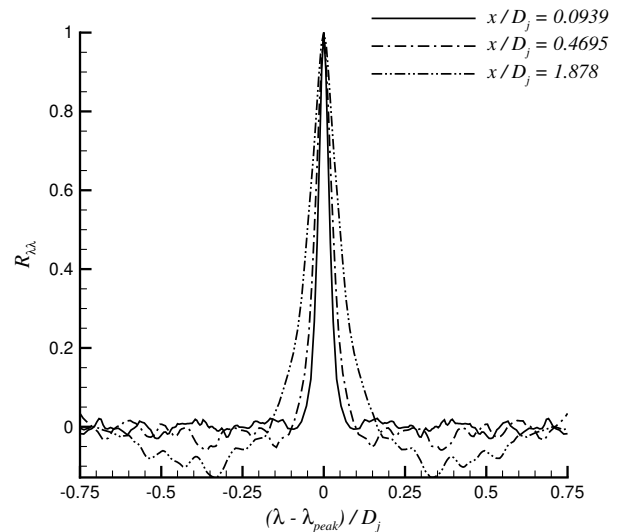


Fig. 30 Two-point correlations of the λ direction velocity $R_{\lambda\lambda}$ at the half-velocity point in the maximum shear-layer thickness location.

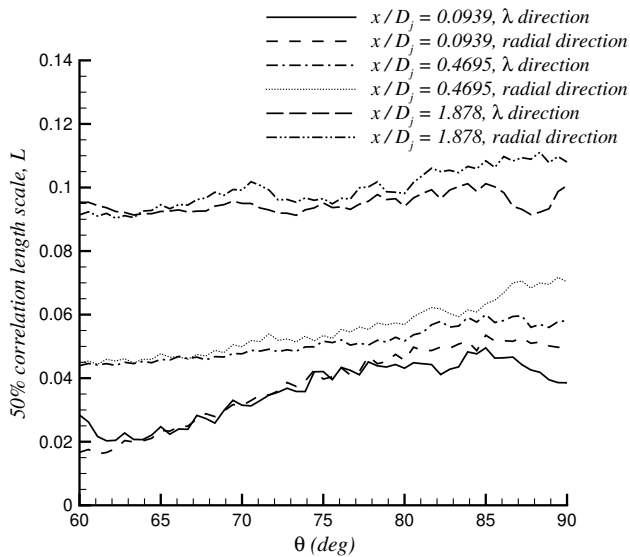


Fig. 31 Comparison of the radial and λ direction length scales along the half-velocity line.

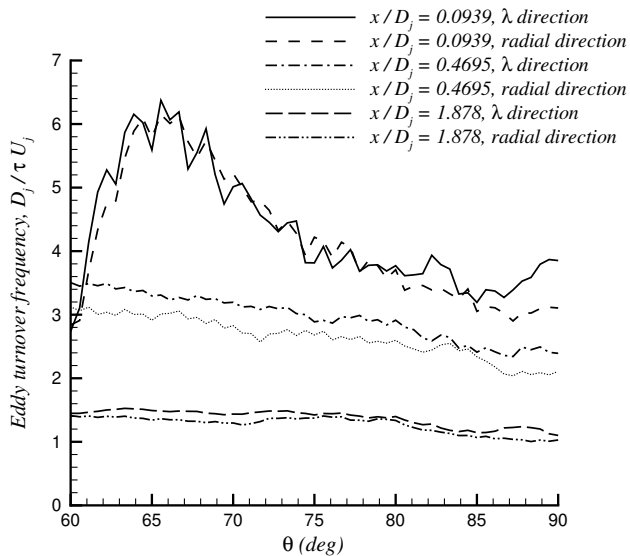


Fig. 32 Comparison of the radial and λ direction eddy turnover frequencies along the half-velocity line.

two directions. It is seen that, in the middle of the mixing layer on a given axial plane, the eddy turnover frequencies for the two directions are comparable to each other as well. The frequencies are highest in the first axial plane, which is located very close to the nozzle exit, and decay with axial distance. The fact that the length scales in the two directions and their corresponding eddy turnover frequencies in the middle of the mixing layer on a given axial plane are comparable to each other must be a direct consequence of the enhanced shear-layer mixing. In contrast, for a round jet mixing layer, it was previously shown that the radial length scale on the nozzle lip line is about 3 times the size of the azimuthal length scale, whereas the azimuthal turnover frequency on the nozzle lip line is roughly 3 times the radial turnover frequency in the near-nozzle region [9]. Thus, for the round jet mixing layer, in the middle of the mixing layer, the azimuthal length scale is the smallest length scale and has the highest eddy turnover frequency. On the other hand, in the middle of the chevron jet mixing layer, the size of the local λ direction length scale, which is analogous to the azimuthal length scale in the round jet mixing layer, and its corresponding time scale (or eddy turnover frequency) are comparable to the size of the local radial

length scale and its corresponding time scale (or eddy turnover frequency), respectively.

C. Estimation of Grid Size Needed for a Simulation at Experimental Reynolds Number

We will now estimate the number of grid points needed for the simulation of a chevron nozzle jet for which the Reynolds number exactly matches that of the experiment. We shall denote this hypothetical new simulation as LES-BigRe. The current computation on the 100 million grid will be called LES-SmallRe.

In LES-SmallRe, we used 113 points in the axial direction within the nozzle, 649 points in the azimuthal direction, and 101 points in the wall-normal direction. The nozzle boundary layers in LES-SmallRe contained 50–60 points in the wall-normal direction. Because the Reynolds number of LES-BigRe is 14 times that of LES-SmallRe, we estimate that the LES-SmallRe grid would need to be refined roughly 10 times in the axial and azimuthal directions to get reasonable boundary-layer resolutions in wall units for LES-BigRe. Thus, we see that we would need about 6500 points in the azimuthal direction and 1130 points in the axial direction within the nozzle. In LES-SmallRe, we had 50–60 points within the boundary layer. To maintain similar wall-normal grid spacings (in wall units) in LES-BigRe, we would need to use approximately 5 times as many grid points within the boundary layer. We assume that a total number of 400 points in the wall-normal direction, of which roughly 300 would be located within the boundary layer, will be sufficient. Thus, LES-BigRe would have to contain about 2.9 billion grid points within the nozzle alone.

Next, we focus on the region outside the nozzle. In LES-SmallRe, we used about 250 points in the axial direction to cover the region from the nozzle exit to roughly four diameters downstream of the nozzle exit. We also used another 40 streamwise points in the sponge zone. The sponge zone is about three nozzle diameters long. Thus, we had about 290 points in the axial direction in the region downstream of the nozzle exit. In the bulk of the free shear-layer region, the axial grid spacing corresponded to about 100 wall units. To maintain similar axial grid spacings (in wall units) in the shear layer of LES-BigRe, we again see that we would need to refine our LES-SmallRe grid by a factor of 10 in the axial direction outside the nozzle.

The number of azimuthal points outside the nozzle will be kept the same as that within the nozzle, that is, roughly 6500 points. Although the nozzle grid only discretizes the core region of the jet using 400 points in the radial direction, the grid outside the nozzle would need additional points in the radial direction to discretize the mixing layer, which expands with axial distance. In LES-SmallRe, the total number of grid points in the radial direction (including the jet core and the mixing layer region) was about 385. With a factor of 5 radial grid refinement in the mixing layer region, we see that we roughly need about 1925 points total in the radial direction in the mixing region.

Thus, we see that we would need about 2900 points in the axial direction, 6500 points in the azimuthal direction, and 1925 points in the radial direction in the region downstream of the nozzle. This corresponds to roughly 36.3 billion points in the free shear-layer region. Adding this to the nozzle interior grid, we see that we would need almost 40 billion grid points total for the near-nozzle simulation of a chevron jet at a Reynolds number of 1.4 million. It should be reiterated that this region extends only 4 diameters downstream of the nozzle exit. Additional grid points would be needed to extend the domain further downstream.

To compute the high-frequency noise propagation to the sideline direction, we would need to surround the near field of the jet flow with a relatively coarser acoustic grid. The purpose of the acoustic grid is to accurately capture the linear acoustic wave propagation outside the jet mixing layers. The control surface needed for the FWH method, which is a surface integral acoustics method, will be located within the acoustic grid. Time-accurate data to be gathered on this control surface will be used to compute noise propagation to the far field. The size of the acoustic grid would be on the order of several

hundred million points at most. Thus, the size of this grid is negligible compared with the main near-nozzle region grid.

For LES-Small Re , using 512 cores (or processors) in parallel on a 100-million-point grid, the LES code needs about 20 days of runtime to run a total of 100,000 time steps total on the present day fastest supercomputers. In LES-Small Re , each core or processor works on roughly 195,000 points. For LES-Big Re , another thing to note is that the computational time step would have to be 10 times smaller because the wall-normal grid spacing is roughly 10 times smaller than that in LES-Small Re . Thus, LES-Big Re would have to be run 10 times longer. Now, assuming that the processor execution speeds a few years from now are roughly 10 times faster than that of today, this means that to run 1 million time steps on a 40-billion-point grid, one would require about 205,000 cores or processors (=40 billion points/195,000 points per core). Such a simulation would take about 20 days to run 1 million time steps.

IV. Conclusions

A unique computation that focuses solely on the noise generation in the near-nozzle region of a jet exhausting from a chevron nozzle has been performed. Both flowfield and acoustics results were compared with available experimental data. Turbulence intensity comparisons showed good agreement on the fifth and sixth PIV planes, whereas good mean axial velocity comparisons were observed starting on the third PIV plane. Comparisons of the turbulence intensities on the first four PIV planes located within the first diameter of the nozzle exit plane were not quite fruitful because the experimental measurements in that region are rather questionable.

The comparison of the noise spectra in the sideline direction showed that the spectrum obtained using the 100-million-point grid is very encouraging and captures much of the frequency range rather well. The computation on the coarser grid also captured the lower frequency region fairly well, yet its prediction in the very high-frequency range was poor. Some of the possible reasons for the differences observed in the very high-frequency range were explained. Because of the relatively short streamwise domain size, the LES acoustics predictions in the low-frequency range should be looked upon with some caution. A new simulation on a longer streamwise domain would be very helpful to clarify some of the discussed issues.

An analysis of the length and time scales in the middle of the chevron jet mixing layer revealed the fact that the local radial length scale and its eddy turnover frequency are roughly equal to the local λ direction length scale and its eddy turnover frequency, respectively. This is believed to be a consequence of the enhanced shear-layer mixing caused by the chevron-induced axial vorticity.

Overall, the simulation results are very encouraging and demonstrate the feasibility of chevron nozzle jet computations using our simulation methodology. The fact that the boundary layer feeding into the chevron nozzle is in a transitional rather than fully turbulent state is a pending issue.

Acknowledgments

This research is sponsored by NASA John H. Glenn Research Center. Nicholas Georgiadis serves as the technical monitor. This work is also partially supported by the National Center for Supercomputing Applications and the Pittsburgh Supercomputing Center under the TeraGrid Grant MCA06N043. Computations used the National Center for Supercomputing Applications Xeon Linux Cluster and the Pittsburgh Supercomputing Center Cray XT3 system. We thank James Bridges and Abbas Khavaran for providing the experimental measurements. We also acknowledge useful discussions with Stanley Birch, Philippe Spalart, and David Lockard.

References

- [1] Bridges, J., and Brown, C. A., "Parametric Testing of Chevrons on Single Flow Hot Jets," NASA TM 2004-213107; also AIAA Paper 2004-2824, 2004.
- [2] Engblom, W. A., Khavaran, A., and Bridges, J., "Numerical Prediction of Chevron Nozzle Noise Reduction Using WIND-MGBK Methodology," AIAA Paper 2004-2479, 2004.
- [3] Birch, S. F., Lyubimov, D. A., Maslov, V. P., and Secundov, A. N., "Noise Prediction for Chevron Nozzle Flows," AIAA Paper 2006-2600, 2006.
- [4] Massey, S. J., Elmiligui, A. A., Hunter, C. A., Thomas, R. H., Pao, S. P., and Mengle, V. G., "Computational Analysis of a Chevron Nozzle Uniquely Tailored for Propulsion Airframe Aeroacoustics," AIAA Paper 2006-2436, 2006.
- [5] Mani, R., Glibe, P. R., and Balsa, T. F., "High Velocity Jet Noise Source Location and Reduction," Federal Aviation Admin., Task 2, FAA-RD-76-79-II, 1978.
- [6] Khavaran, A., "Role of Anisotropy in Turbulent Mixing Noise," *AIAA Journal*, Vol. 37, No. 7, July 1999, pp. 832–841. doi:10.2514/2.7531
- [7] Shur, M. L., Spalart, P. R., and Strelets, M. K., "Noise Prediction for Increasingly Complex Jets, Part II: Applications," *International Journal of Aeroacoustics*, Vol. 4, Nos. 3–4, 2005, pp. 247–266. doi:10.1260/1475472054771385
- [8] Shur, M. L., Spalart, P. R., Strelets, M. K., and Garbaruk, A. V., "Further Steps in LES-Based Noise Prediction for Complex Jets," AIAA Paper 2006-485, Jan. 2006.
- [9] Uzun, A., and Hussaini, M. Y., "Investigation of High Frequency Noise Generation in the Near-Nozzle Region of a Jet Using Large Eddy Simulation," *Theoretical and Computational Fluid Dynamics*, Vol. 21, No. 4, 2007, pp. 291–321. doi:10.1007/s00162-007-0048-z
- [10] Uzun, A., Hussaini, M. Y., and Streett, C. L., "Large-Eddy Simulation of a Wing Tip Vortex on Overset Grids," *AIAA Journal*, Vol. 44, No. 6, 2006, pp. 1229–1242. doi:10.2514/1.17999
- [11] Lund, T. S., Wu, X., and Squires, K. D., "Generation of Turbulent Inflow Data for Spatially-Developing Boundary Layer Simulations," *Journal of Computational Physics*, Vol. 140, No. 2, 1998, pp. 233–258. doi:10.1006/jcph.1998.5882
- [12] Rizzetta, D. P., Visbal, M. R., and Blaisdell, G. A., "A Time-Implicit High-Order Compact Differencing and Filtering Scheme for Large-Eddy Simulation," *International Journal for Numerical Methods in Fluids*, Vol. 42, No. 6, 2003, pp. 665–693. doi:10.1002/flid.551
- [13] Uzun, A., "3-D Large Eddy Simulation for Jet Aeroacoustics," Ph.D. Thesis, School of Aeronautics and Astronautics, Purdue Univ., West Lafayette, IN, Dec. 2003.
- [14] Uzun, A., Blaisdell, G. A., and Lyrantzis, A. S., "Application of Compact Schemes to Large Eddy Simulation of Turbulent Jets," *Journal of Scientific Computing*, Vol. 21, No. 3, Dec. 2004, pp. 283–319. doi:10.1007/s10915-004-1319-0
- [15] Uzun, A., Lyrantzis, A. S., and Blaisdell, G. A., "Coupling of Integral Acoustics Methods with LES for Jet Noise Prediction," *International Journal of Aeroacoustics*, Vol. 3, No. 4, Oct. 2004, pp. 297–346. doi:10.1260/1475472043499290
- [16] Gaitonde, D. V., and Visbal, M. R., "Padé-Type Higher-Order Boundary Filters for the Navier–Stokes Equations," *AIAA Journal*, Vol. 38, No. 11, Nov. 2000, pp. 2103–2112. doi:10.2514/2.872
- [17] Visbal, M. R., and Gaitonde, D. V., "Very High-Order Spatially Implicit Schemes for Computational Acoustics on Curvilinear Meshes," *Journal of Computational Acoustics*, Vol. 9, No. 4, 2001, pp. 1259–1286.
- [18] Ashcroft, G., and Zhang, X., "Optimized Prefactored Compact Schemes," *Journal of Computational Physics*, Vol. 190, No. 2, 2003, pp. 459–477. doi:10.1016/S0021-9991(03)00293-6
- [19] Lele, S. K., "Compact Finite Difference Schemes with Spectral-Like Resolution," *Journal of Computational Physics*, Vol. 103, No. 1, Nov. 1992, pp. 16–42. doi:10.1016/0021-9991(92)90324-R
- [20] Beam, R. M., and Warming, R. F., "An Implicit Factored Scheme for the Compressible Navier–Stokes Equations," *AIAA Journal*, Vol. 16, No. 4, April 1978, pp. 393–402. doi:10.2514/3.60901
- [21] Ekaterinaris, J. A., "Implicit, High-Resolution, Compact Schemes for Gas Dynamics and Aeroacoustics," *Journal of Computational Physics*, Vol. 156, No. 2, 1999, pp. 272–299. doi:10.1006/jcph.1999.6360
- [22] Pulliam, T. H., "Artificial Dissipation Models for the Euler Equations," *AIAA Journal*, Vol. 24, No. 12, Dec. 1986, pp. 1931–1940. doi:10.2514/3.9550

- [23] Sagaut, P., Garnier, E., Tromeur, E., Larchevêque, L., and Labourasse, E., "Turbulent Inflow Conditions for Large-Eddy Simulation of Compressible Wall-Bounded Flows," *AIAA Journal*, Vol. 42, No. 3, March 2004, pp. 469–477.
doi:10.2514/1.3461
- [24] Spalding, D. B., "A Single Formula for the Law of the Wall," *Journal of Applied Mechanics*, Vol. 28, Sept. 1961, pp. 455–458.
- [25] Dong, T. Z., "On Boundary Conditions for Acoustic Computations in Non-Uniform Mean Flows," *Journal of Computational Acoustics*, Vol. 5, No. 3, 1997, pp. 297–315.
doi:10.1142/S0218396X97000174
- [26] Tam, C. K. W., and Dong, Z., "Radiation and Outflow Boundary Conditions for Direct Computation of Acoustic and Flow Disturbances in a Nonuniform Mean Flow," *Journal of Computational Acoustics*, Vol. 4, No. 2, 1996, pp. 175–201.
doi:10.1142/S0218396X96000040
- [27] Kim, J. W., and Lee, D. J., "Generalized Characteristic Boundary Conditions for Computational Aeroacoustics," *AIAA Journal*, Vol. 38, No. 11, Nov. 2000, pp. 2040–2049.
doi:10.2514/2.891
- [28] Kim, J. W., and Lee, D. J., "Generalized Characteristic Boundary Conditions for Computational Aeroacoustics, Part 2," *AIAA Journal*, Vol. 42, No. 1, Jan. 2004, pp. 47–55.
doi:10.2514/1.9029
- [29] Visbal, M. R., and Rizzetta, D. P., "Large-Eddy Simulation on Curvilinear Grids Using Compact Differencing and Filtering Schemes," *Journal of Fluids Engineering*, Vol. 124, No. 4, Dec. 2002, pp. 836–847.
doi:10.1115/1.1517564
- [30] Visbal, M. R., Morgan, P. E., and Rizzetta, D. P., "An Implicit LES Approach Based on High-Order Compact Differencing and Filtering Schemes (Invited)," *AIAA Paper 2003-4098*, June 2003.
- [31] Sherer, S. E., and Visbal, M. R., "Implicit Large Eddy Simulations Using a High-Order Overset Grid Solver," *AIAA Paper 2004-2530*, July 2004.
- [32] Sherer, S. E., and Scott, J. N., "High-Order Compact Finite-Difference Methods on General Overset Grids," *Journal of Computational Physics*, Vol. 210, No. 2, Dec. 2005, pp. 459–496.
doi:10.1016/j.jcp.2005.04.017
- [33] Lyrintzis, A. S., "Surface Integral Methods in Computational Aeroacoustics: From the (CFD) Near-Field to the (Acoustic) Far-Field," *International Journal of Aeroacoustics*, Vol. 2, No. 2, 2003, pp. 95–128.
- [34] Choi, H., and Moin, P., "Effects of the Computational Time Step on Numerical Solutions of Turbulent Flow," *Journal of Computational Physics*, Vol. 113, No. 1, July 1994, pp. 1–4.
doi:10.1006/jcph.1994.1112
- [35] Freund, J. B., Lele, S. K., and Moin, P., "Calculation of the Radiated Sound Field Using an Open Kirchhoff Surface," *AIAA Journal*, Vol. 34, No. 5, May 1996, pp. 909–916.
doi:10.2514/3.13167
- [36] Spalart, P. R., "Direct Simulation of a Turbulent Boundary Layer up to $Re_\theta = 1410$," *Journal of Fluid Mechanics*, Vol. 187, No. 1, 1988, pp. 61–98.
doi:10.1017/S0022112088000345
- [37] Rai, M. M., and Moin, P., "Direct Numerical Simulation of Transition and Turbulence in a Spatially Evolving Boundary Layer," *Journal of Computational Physics*, Vol. 109, No. 2, Dec. 1993, pp. 169–192.
doi:10.1006/jcph.1993.1210
- [38] Spalart, P. R., Strelets, M., and Travin, A., "Direct Numerical Simulation of Large-Eddy-Break-Up Devices in a Boundary Layer," *International Journal of Heat and Fluid Flow*, Vol. 27, No. 5, Oct. 2006, pp. 902–910.
doi:10.1016/j.ijheatfluidflow.2006.03.014
- [39] Narayanan, S., Barber, T. J., and Polak, D. R., "High Subsonic Jet Experiments: Turbulence and Noise Generation Studies," *AIAA Journal*, Vol. 40, No. 3, 2002, pp. 430–437.
doi:10.2514/2.1692

D. Gaitonde
Associate Editor